

This work was written as part of one of the author's official duties as an Employee of the United States Government and is therefore a work of the United States Government. In accordance with 17 U.S.C. 105, no copyright protection is available for such works under U.S. Law.

Public Domain Mark 1.0

<https://creativecommons.org/publicdomain/mark/1.0/>

Access to this work was provided by the University of Maryland, Baltimore County (UMBC) ScholarWorks@UMBC digital repository on the Maryland Shared Open Access (MD-SOAR) platform.

**Please provide feedback**

Please support the ScholarWorks@UMBC repository by emailing [scholarworks-group@umbc.edu](mailto:scholarworks-group@umbc.edu) and telling us what having access to this work means to you and why it's important to you. Thank you.



## Multiscale Observations of Hurricane Dennis (2005): The Effects of Hot Towers on Rapid Intensification

STEPHEN R. GUIMOND

*Center for Ocean–Atmospheric Prediction Studies and Department of Meteorology,  
The Florida State University, Tallahassee, Florida*

GERALD M. HEYMSFIELD

*NASA Goddard Space Flight Center, Greenbelt, Maryland*

F. JOSEPH TURK\*

*Naval Research Laboratory, Monterey, California*

(Manuscript received 26 February 2009, in final form 26 August 2009)

### ABSTRACT

A synthesis of remote sensing and in situ observations throughout the life cycle of Hurricane Dennis (2005) during the NASA Tropical Cloud Systems and Processes (TCSP) experiment is presented. Measurements from the ER-2 Doppler radar (EDOP), the Advanced Microwave Sounding Unit (AMSU), airborne radiometer, and flight-level instruments are used to provide a multiscale examination of the storm. The main focus is an episode of deep convective bursts (“hot towers”) occurring during a mature stage of the storm and preceding a period of rapid intensification (11-hPa pressure drop in 1 h 35 min). The vigorous hot towers penetrated to 16-km height, had maximum updrafts of  $20 \text{ m s}^{-1}$  at 12–14-km height, and possessed a strong transverse circulation through the core of the convection. Significant downdrafts (maximum of  $10\text{--}12 \text{ m s}^{-1}$ ) on the flanks of the updrafts were observed, with their cumulative effects hypothesized to result in the observed increases in the warm core. In one ER-2 overpass, subsidence was transported toward the eye by  $15\text{--}20 \text{ m s}^{-1}$  inflow occurring over a deep layer (0.5–10 km) coincident with a hot tower.

Fourier analysis of the AMSU satellite measurements revealed a large shift in the storm’s warm core structure, from asymmetric to axisymmetric,  $\sim 12 \text{ h}$  after the convective bursts began. In addition, flight-level wind calculations of the axisymmetric tangential velocity and inertial stability showed a contraction of the maximum winds and an increase in the stiffness of the vortex, respectively, after the EDOP observations.

The multiscale observations presented here reveal unique, ultra-high-resolution details of hot towers and their coupling to the parent vortex, the balanced dynamics of which can be generally explained by the axisymmetrization and efficiency theories.

## 1. Introduction

### *a. Instruments for tropical cyclone observation*

Advancements in the field of atmospheric science (and science in general) often arise because of new and inno-

vative observations of the entity being studied. Such is the case with the problem of tropical cyclone (TC) intensification. In recent years, the plethora of instruments (e.g., dropsondes, aircraft Doppler radars, microwave satellite imagers and sounders) has led to an increase in the frequency and quality of TC inner core observations, providing improvement in the forecasting of TC evolution (Kepert et al. 2006). For example, the use of passive microwave instruments mounted on a variety of satellites has assisted in the monitoring of eyewall replacement cycles, one important aspect of the intensification process (Willoughby et al. 1982; Hawkins et al. 2006; Jones et al. 2006). In addition, the Advanced Microwave Sounding

---

\* Current affiliation: Jet Propulsion Laboratory, Pasadena, California.

---

*Corresponding author address:* Stephen R. Guimond, Center for Ocean–Atmospheric Prediction Studies, The Florida State University, Tallahassee, FL 32310.  
E-mail: guimond@coaps.fsu.edu

Unit (AMSU) series of satellites has assisted researchers and forecasters alike through the ability to monitor the three-dimensional (3D) warm core of a TC, another important aspect of intensification that leads directly to lowered surface pressures and increased winds through thermal wind adjustment (Kidder et al. 2000; Spencer and Braswell 2001; Brueske and Velden 2003; Knaff et al. 2004).

Airborne Doppler radar has arguably had the most extensive and fruitful role in TC research, particularly in the observation of storm structure and dynamics. For thirty years, the National Oceanic and Atmospheric Administration (NOAA) WP-3D (P-3) aircraft have been providing a wealth of details on TCs that has revolutionized the understanding and operational forecasting of these systems (e.g., Jorgensen 1984; Marks and Houze 1987; Aberson et al. 2006; Reasor et al. 2009). In addition to the P-3 TA radar, the more advanced Electra Doppler Radar (ELDORA) operated by the National Center for Atmospheric Research (NCAR) has flown recent missions into TCs revealing convective-scale detail in rainband and inner core regions (Houze et al. 2006). A unique radar system providing some of the highest-quality vertical velocity estimates in several TCs is the National Aeronautics and Space Administration (NASA) ER-2 Doppler radar (EDOP), which is the focus of this study.

Each of the above airborne Doppler radar platforms has positive and negative attributes associated with measuring atmospheric phenomena (such as TCs). Central to these attributes are details of the scanning geometry and effective resolution, which will be discussed in greater depth in section 2b.

### *b. Hot towers*

Several decades of research have highlighted the role of horizontally small, intense cores of rapidly rising, nearly undiluted air that reach and/or penetrate the tropopause (“hot towers” or HTs) in the tropical atmosphere, including TCs (Riehl and Malkus 1958; Malkus and Riehl 1960; Gentry et al. 1970; Steranka et al. 1986; Simpson et al. 1998; Heymsfield et al. 2001; Kelley et al. 2004; Hendricks et al. 2004; Montgomery et al. 2006). Although hot towers have been studied sporadically for quite some time, many more details are yet to be observed and understood about these complex yet seemingly important features within the TC life cycle. In the last decade, there has been a resurgence of interest in hot towers (and deep convective bursts) in TCs, with new observational information uncovered (Reasor et al. 2009; Houze et al. 2009) and theories on how they fit into the TC genesis and intensification problems presented (Montgomery and Enagonio 1998;

Möller and Montgomery 1999; Nolan and Grasso 2003; Nolan et al. 2007). Despite the focus on hot towers, several studies have shown that net heating drives TC intensification (i.e., Cecil and Zipser 1999; Tory et al. 2006), although there is evidence that decaying convective bursts (or hot towers) can produce a large amount of stratiform heating in addition to convective heating (Houze et al. 2009).

Hot towers occurring in an environment of sufficient background rotation generate potential vorticity (PV) anomalies through (i) transport of high-entropy ( $\theta_e$ ) air extracted at the ocean surface leading to a release of latent heat aloft and (ii) tilting and stretching of ambient vorticity by strong updrafts in the core (“vortical hot towers” or VHTs; Hendricks et al. 2004; Montgomery et al. 2006). The updraft appears to be the most important feature of the VHT, providing a medium for  $\theta_e$  transport and formation of large, collocated vertical vorticity anomalies (i.e., rotating updraft).

Using the P-3 TA radar in vertical incidence ( $\sim 750$ -m along-track sampling), Black et al. (1996) found maximum vertical velocities between 10 and 26  $\text{m s}^{-1}$  in seven intense Atlantic hurricanes with  $\sim 5\%$  of eyewall updrafts  $> 5 \text{ m s}^{-1}$ . Heymsfield et al. (2010) compiled 13 vertical velocity profiles of deep convection (defined as updrafts  $> 10 \text{ m s}^{-1}$  over at least a kilometer along track) in hurricanes and found that the peak value of the mean profile was  $\sim 13\text{--}14 \text{ m s}^{-1}$ . The updrafts we analyze in this paper are larger than this; thus, we define hot towers as a special class of deep convection [the largest peak updrafts in the Black et al. (1996) and Heymsfield et al. (2010) populations]. There is evidence that downdrafts play an important role in HTs and VHTs as well. Heymsfield et al. (2001) analyzed EDOP data from Hurricane Bonnie (1998) and found a deep, broad subsidence current on the inner edge of a HT that they hypothesized played a large role in the development of the warm core.

In general, the PV anomalies associated with an asymmetric distribution of HTs (or VHTs) are axisymmetrized into the parent circulation via vortex Rossby wave dynamics (Montgomery and Kallenbach 1997; Montgomery and Enagonio 1998). In their cyclogenesis experiments, Montgomery and Enagonio (1998) showed how convectively induced eddy heat and momentum fluxes (a by-product of vortex Rossby waves) can force the development of subsidence near the center of the vortex, yielding growth of the warm core. Similarly, Willoughby (1998) presented a conceptual model, based on observations, for the intensification of the warm core whereby deep convection acts to draw mass from the low-level eye into the eyewall, forcing subsidence at the center of the vortex. Schubert and Hack (1982) found, using

an analytical approach, that the efficiency of the above processes (the ratio of local warming to convective heating) is highly dependent on the inertial stability of the background vortex. Large increases in the efficiency and intensification were found to scale with increases in the inertial stability, a result of the vortex's ability to resist radial parcel displacements and concentrate the transverse circulation (Eliassen 1951; Shapiro and Willoughby 1982; Schubert and Hack 1982; Nolan et al. 2007).

In this paper, we examine the life cycle of Hurricane Dennis (2005) with a focus on an outbreak of HTs during a mature stage of the storm just prior to a period of rapid intensification. The purpose of this study is to document unique observations (EDOP and others) of HTs and fit them, using observations, into the larger-scale evolution of the vortex. We study the thermodynamics and dynamics of the vortex by using satellite and in situ measurements and discuss how their interplay with the new HT observations can be explained in terms of the theory discussed above.

## 2. Data and processing

### a. AMSU

The AMSU is a cross-track scanning microwave radiometer operating primarily through 12 channels in the oxygen absorption band (50–60 GHz) with a swath width of 2179 km and horizontal resolution near nadir of 48 km (Kidder et al. 2000). Because of the relatively coarse resolution, the AMSU can only resolve the large-scale warm anomaly of a TC; however, the routine operational use of these data for estimating TC intensity at the National Hurricane Center (NHC) demonstrates the utility of these measurements (J. Knaff and C. Velden 2008, personal communication). Although HTs are not resolvable by the AMSU, it is expected that the collective effects of multiple HTs (i.e., a convective burst) will be discernable in the data because of the large amount of diabatic heating, subsidence, and attendant falling surface pressure that both theory and observations show following convective burst episodes (Shapiro and Willoughby 1982; Montgomery and Enagonio 1998; Heymsfield et al. 2001; Kelley et al. 2004).

Retrievals of AMSU temperature profiles are provided by the Cooperative Institute for Research in the Atmosphere (CIRA) following the procedures outlined in Goldberg et al. (2001) and Demuth et al. (2004). Important steps in the retrievals are the corrections for antenna side lobes, adjustment of off-nadir scan angles to nadir incidence, statistical determination of temperature as a function of pressure, and correction for

hydrometeor contamination (radiation that is attenuated by cloud liquid water and scattered by ice particles). Demuth et al. (2004) only apply cloud liquid water and ice corrections from 350 hPa and below. Cloud liquid water effects above 350 hPa are essentially zero (Demuth et al. 2004). Furthermore, an independent analysis revealed very little ice scattering above 350 hPa (for AMSU footprints), especially at and above 200 hPa where we focus our study, essentially confirming the analysis of Demuth et al. (2004).

To apply the hydrometeor corrections from 350 hPa and below, the data are first interpolated from the native swath grid to a Cartesian grid with uniform  $0.2^\circ$  spacing using a distance-weighted averaging method. This procedure utilizes an  $e$ -folding radius (100 km; Demuth et al. 2004) that smoothes the temperature fields. The smoothing is applied on the entire volume of data (including above 350 hPa). An examination of raw (unsmoothed) versus corrected (smoothed) temperature fields at 200 hPa revealed large discrepancies (raw fields were  $\sim 2.5$  K larger) in the warm anomaly of Hurricane Dennis. Thus, the intensity of a TC has the potential to be significantly underestimated using the present hydrometeor correction procedure (a comprehensive evaluation of this problem is currently underway). To avoid many of these problems, the raw temperatures in the 100–300-hPa layer (mostly 200 hPa) on the native swath are analyzed in this paper. These raw temperatures will still underestimate the warm core of a TC because of the resolution limitations, but the magnitudes are much larger than those using the Demuth et al. (2004) algorithm. The root-mean-square errors for the raw retrievals (removed from heavy precipitation) are less than  $2^\circ\text{C}$  (Goldberg 1999; Kidder et al. 2000).

### b. EDOP

The EDOP is an X-band (9.6 GHz) Doppler radar with fixed nadir and forward ( $33^\circ$  off nadir) beams, each with a  $2.9^\circ$  beamwidth. Measurements are taken from the high-altitude (20 km) ER-2 aircraft every 0.5 s with a  $200\text{ m s}^{-1}$  ground speed providing some of the finest sampling of any current airborne radar (100 m along track with a typical 37.5-m gate spacing; Heymsfield et al. 1996). The along-track spacing results in significant oversampling of precipitation, yielding an effective horizontal resolution between 100 m and the  $2.9^\circ$  beamwidth (i.e.,  $\sim 0.55$  km at the surface and  $\sim 0.30$  km at 10-km altitude).

The main advantage of EDOP is the nadir-viewing geometry that provides direct measurements of the vertical component of Doppler velocities relative to the aircraft and superior resolution when compared to the P-3s and ELDORA. For example, the along-track

*sampling* of the P-3 tail (TA) radar in normal-plane scanning mode and fore/aft (FAST) scanning mode is  $\sim 0.75$  km and  $\sim 1.5$  km, respectively, with 0.15-km gate spacing (Gamache et al. 1995; Black et al. 1996). Taking into account the  $1.9^\circ$  vertical and  $1.35^\circ$  horizontal beamwidths of the TA antenna and the sampling intervals using FAST, grid resolutions from the P-3s range from 1.5–2.0 km in the horizontal to 0.5–1.0 km in the vertical (Reasor et al. 2000, 2009). The scanning geometry of ELDORA is similar to that of the P-3 TA radar with the exception of a faster antenna rotation rate yielding finer along-track sampling of  $\sim 0.4$  km. A typical gate spacing for ELDORA is 0.15 km, which when combined with the  $1.8^\circ$  beamwidth results in grid resolutions of  $\sim 0.4$  km in the horizontal and 0.3 km in the vertical (Hildebrand et al. 1996; Wakimoto et al. 1996).

Another advantage of EDOP measurements is the ability of the ER-2 to overfly intense convection (such as HTs) with a quasi-stable platform, whereas other aircraft typically rely on side-looking views of high reflectivity regions because of safety concerns (Heymsfield et al. 1996). The main disadvantage in using EDOP is the inability to retrieve 3D winds, as the nonscanning beams only measure Doppler velocities along the vertical plane of the aircraft track.

The removal of aircraft motions and mapping to an earth-fixed reference frame are completed following Lee et al. (1994). Next, the nadir and forward beams are interpolated to a common grid (100 m horizontal, 37.5 m vertical) and the equations for the vertical and along-track velocities outlined in Heymsfield et al. (1996) are solved. Finally, an estimation of hydrometeor fall speeds is computed based on a gamma raindrop size distribution (Ulbrich and Chilson 1994) and the reflectivity relationships tuned for the EDOP described in Heymsfield et al. (1999).

Gamma distributions are found to be significantly better (Heymsfield et al. 1999) than the power-law reflectivity–fall speed relationships typically used in TC studies (i.e., Marks and Houze 1987; Reasor et al. 2009). Before the relationships are applied, the nadir beam reflectivity is corrected for attenuation using the surface reference technique (Iguchi and Meneghini 1994). Although the characterization of fall speeds is an underdetermined problem, we take these extra steps because uncertainties in fall speeds translate directly to errors in vertical velocities of several meters per second in the mixed-phase regions of convection. The along-track winds are more accurate than the vertical winds because of their independence on fall speeds, although minor sensitivity to data filtering was found (filtering was not done here to preserve raw magnitudes).

### c. AMPR

In addition to EDOP, the ER-2 carried the Advanced Microwave Precipitation Radiometer (AMPR), a cross-track scanning ( $\pm 45^\circ$  about nadir) microwave radiometer sensing upwelling radiation at several frequencies (10.7, 19.35, 37.1, and 85.5 GHz) ideal for studying the liquid and ice phases of deep convection (Spencer et al. 1994; Turk et al. 1998; Hood et al. 2006). At 20-km altitude, the AMPR maintains a 40-km swath width at the surface with a horizontal resolution at nadir between 640 m for the 85-GHz channel and 2.8 km for the 10-GHz channel (Hood et al. 2006). Figure 1 displays a schematic of the EDOP and AMPR sampling geometries onboard the high-altitude ER-2.

### d. Flight-level data

Quality-controlled (“ten-second files”; sampling frequency of 0.1 and 1.0 Hz) flight-level winds from two NOAA P-3 aircraft and several United States Air Force (USAF) WC-130 aircraft provided by the Hurricane Research Division (HRD) were used to analyze the storm-relative, tangential wind over the life cycle of Dennis. Detailed descriptions of the data processing and instrumentation onboard these aircraft can be found in Jorgensen (1984). The flight-level winds were converted to storm-relative tangential velocities as follows. First, the center of circulation in the flight-level measurements was found by minimizing the separation (in space and time) between storm center estimates from Willoughby and Chelmow (1982) and the aircraft radial passes through the storm. Second, an estimate of storm motion was computed from the Willoughby and Chelmow (1982) centers and removed from the winds. Finally, a coordinate transformation was applied. The data were then interpolated to a radial grid extending from the center of rotation out to 60 km with 1-km grid spacing and smoothed with a 4-km (five point) running mean. The tangential winds are accurate to within  $1\text{--}2\text{ m s}^{-1}$  (OFCM 1993) and are found to be insensitive to small storm center perturbations. The mean height of the P3 and USAF aircraft were  $\sim 3.6$  km (650 hPa) and  $\sim 3$  km (700 hPa), respectively.

## 3. Overview of Hurricane Dennis

During the summer of 2005, NASA conducted the Tropical Cloud Systems and Processes (TCSP) field experiment in the Caribbean, Gulf of Mexico, and eastern Pacific Ocean basins with the purpose of discovering new insights into the life cycle of TCs (Halverson et al. 2007). Hurricane Dennis tracked through this region in early July, forming from a tropical wave in the eastern

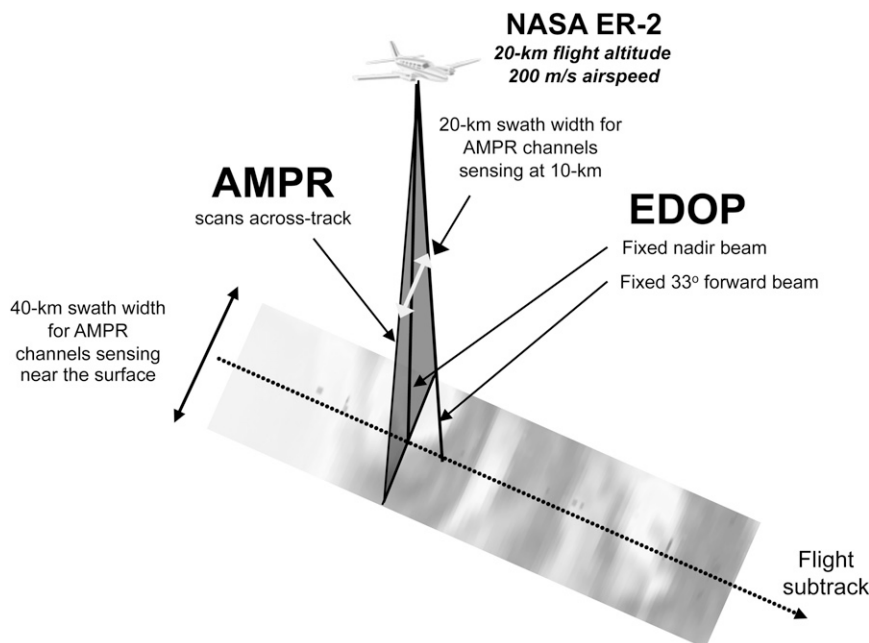


FIG. 1. Configuration of the AMPR and EDOP instruments onboard the ER-2 aircraft revealing a passive microwave scene during TCSP.

Caribbean and growing to a category-4 hurricane before weakening over Cuba. Dennis then emerged into the Gulf of Mexico at 0900 UTC 9 July as a category-1 storm and rapidly intensified to category-4 status, making a final landfall in the western Florida Panhandle at 1930 UTC 10 July (Beven 2005). Figure 2 shows the best track for the life cycle of Hurricane Dennis.

Figure 3 shows the evolution of the maximum sustained winds, minimum surface pressure, and storm-relative, large-scale (500 km, symmetric vortex removed) vertical wind shear (using operational model analyses) for the life cycle of Dennis. Landfall of the system in Cuba occurred late on 8 July and as the system moved into the Gulf of Mexico with sea surface temperatures (SSTs) of 28.5°–29.0°C, the storm began a period of rapid increase in surface winds (Fig. 3a; most notably between 1800 UTC 9 July and 0600 UTC 10 July) just after the high-resolution observations of HTs from EDOP. The central pressure of Dennis (Fig. 3a) was falling at a rate of  $\sim 0.80 \text{ hPa h}^{-1}$  at the time of the ER-2 overpasses, but in the next 15 h the average rate of pressure fall more than doubled to  $\sim 2 \text{ hPa h}^{-1}$ , including an astounding 11-hPa pressure drop in 1 h 35 min ( $\sim 6 \text{ h}$  from the ER-2 overpasses; Beven 2005). The vertical wind shear (Fig. 3b) was elevated before landfall in Cuba and then oscillated between 4 and  $7 \text{ m s}^{-1}$  from the southwest to west-southwest when the storm was located in the Gulf of Mexico. After emerging into the Gulf of Mexico and at the time of the ER-2 overpasses, the storm

had attained only 57% of its empirically derived maximum potential intensity (MPI; DeMaria and Kaplan 1994). The environmental conditions described above (low-shear/weak momentum forcing, high SSTs, and far from MPI) make up a large percentage of the factors that statistically predict rapid intensification as outlined by Kaplan and DeMaria (2003). With a favorable environment in place, we hypothesize that HTs and the inner



FIG. 2. Best-track positions for the life cycle of Hurricane Dennis in July 2005. The thin solid line denotes tropical depression status, the dashed line tropical storm, and the thick solid line hurricane. Open circles mark the 0000 UTC positions. The NASA ER-2 aircraft overpasses of the storm analyzed in this study occurred between 1300 and 1500 UTC 9 Jul.

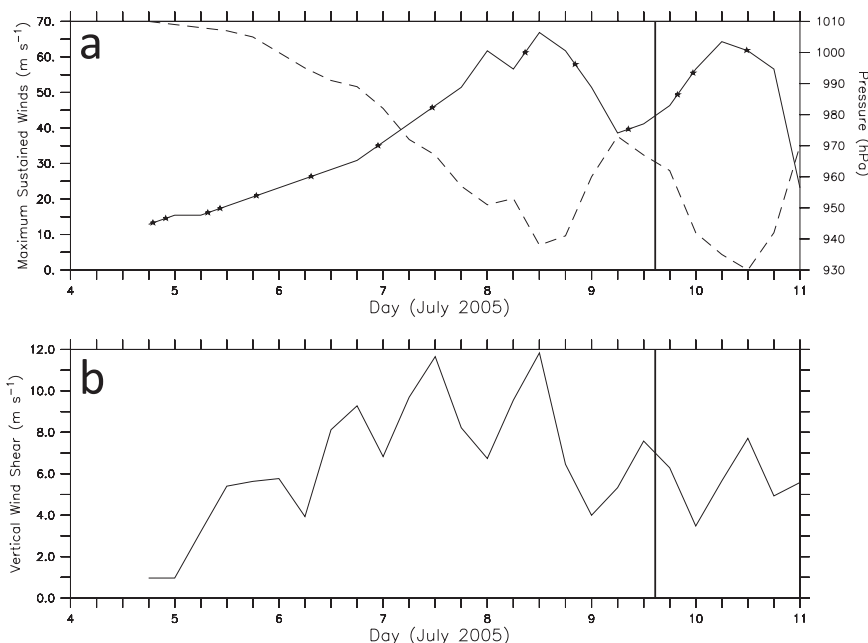


FIG. 3. Time series of (a) maximum sustained winds (solid) and minimum central pressure (dashed) from NHC best-track data and (b) large-scale, storm-relative vertical wind shear magnitude computed from operational model analyses over the life cycle of Hurricane Dennis. The thick black lines mark when the ER-2 sampled the storm and the stars in (a) denote the AMSU overpasses analyzed in this paper.

core dynamics they trigger may be a driving mechanism behind Dennis' transformation.

The stars in Fig. 3a represent the AMSU overpasses of Dennis. A total of 14 quality (storm center and satellite swath center within 600 km) overpasses from several NOAA satellites were synthesized to analyze the development of the warm core from genesis to landfall. Temperature anomalies for each overpass were computed by subtracting out the resting atmosphere temperature (defined as an average over a 600-km radius from the NHC best-track position) from the total temperature. Figure 4 shows the evolution of the maximum temperature anomaly in a column above the storm center. As a result of AMSU's cross-track scanning geometry, the resolution of the footprint decreases as the instrument scans away from nadir (dashed curve in Fig. 4). This effect can obscure physical processes in the storm and result in warm core evolution dictated by footprint resolution. To allow for clearer interpretation, footprint resolutions greater than 65 km are removed from the time series in Fig. 4 and plotted as squares (note that interpolation is used to produce a smooth curve from the remaining footprints in Fig. 4).

It should be noted that data from the High Altitude Monolithic Microwave Integrated Circuits (MMIC) Sounding Radiometer (HAMSR), a high-resolution

microwave sounding radiometer installed in the ER-2, were also analyzed in this study. However, retrievals of temperature were not available and the analysis done on the raw brightness temperatures contained large uncertainty in the derived warm anomaly and was therefore removed.

The AMSU captured much of the evolution of Dennis (shown by the solid curve in Fig. 4), including growth of the storm to a hurricane on 7 July, landfall in Cuba early on 9 July, and the intensification episode after the ER-2 observations. Between 0829 and 2321 UTC 9 July (points from the solid curve in Fig. 4) the AMSU measured an increase of 1.6 K in the warm anomaly; it also measured a 1.8-K increase between 1947 UTC 9 July and 1144 UTC 10 July (points from squares in Fig. 4). We hypothesize that the increases in the warm core on the broad vortex scale shown in the present section are due to the *cumulative* effects of an outbreak of HTs observed in detail in the next section.

#### 4. Hot tower remote sensing observations

Inspection of Geostationary Operational Environmental Satellite (GOES) infrared (IR) animations—a rapid-scan, IR animation on 9 July can be found at <ftp://ftp.coaps.fsu.edu/pub/guimond/dennis1.mov>—for small-scale,

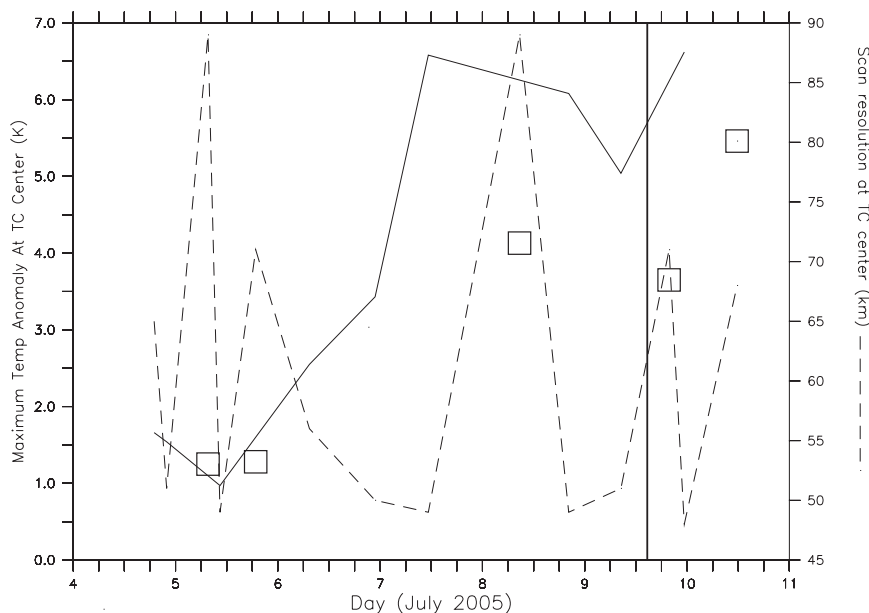


FIG. 4. Time series of Dennis' maximum temperature anomaly in the column above the storm center computed from AMSU overpasses, along with the footprint resolution. The thin black line shows the temperature anomalies for footprint resolutions  $\leq 65$  km (with linear interpolation between data points for a smooth curve). Anomalies for footprint resolutions  $> 65$  km are plotted as squares. The thick black line is as in Fig. 3.

cold cloud tops (proxy for HTs; Heymsfield et al. 2001) revealed an asymmetric distribution of convection oriented in the downshear to downshear left portions of the storm for most of 9 July. The bursts of convection went through an episodic pattern of initiation/growth in the downshear quadrants and rotation upshear where they began to decay. The prevalence for convection to develop in the downshear to downshear left quadrants is a well-recognized phenomena (Frank and Ritchie 2001; Corbosiero and Molinari 2002; Braun et al. 2006; Guimond 2007; Reasor et al. 2009). Figure 5 shows a series of snapshots of one convective burst episode from 1655 to 2210 UTC 9 July that illustrates the above process including the downshear initiation–growth (Fig. 5a) and upshear rotation (Fig. 5b). By around 1910 UTC 9 July (Fig. 5c), the downshear initiation of convection has ceased and the cold cloud tops are being completely wrapped around the storm center with an eye beginning to form. Three hours later (Fig. 5d), the hypothesized aggregate effect of the convective burst episodes has resulted in a strikingly symmetric distribution of cloud tops and the development of a distinct eye that persisted into 10 July.

Zooming in on the ER-2 flight segments between  $\sim 1400$  and 1500 UTC 9 July, Fig. 6 shows 12-min flight segments across Hurricane Dennis from the AMPR 85-GHz channel overlaid on the closest GOES visible satellite imagery. The 85-GHz brightness temperature

( $T_B$ ) depressions are sensitive to radiation scattering by precipitation-sized ice hydrometeors (Spencer et al. 1994). Patches of low  $T_B$  on the eastern (downshear) side of the storm in each panel are observed to begin development during the first two overpasses (Figs. 6a,b). During this time period, the convection appears disorganized and straddles the mean radius of maximum wind (RMW; 25 km) shown as a circle in each panel of Fig. 6. During the third ER-2 overpass (Fig. 6c), the low  $T_B$ 's organized into a thin band inside the mean RMW and dropped to  $\leq 100$  K in  $\sim 20$  min, an indication of strong updrafts lofting large graupel–ice particles to levels where the 85-GHz weighting function peaks in convection (8–10 km). Around 25 min later, Fig. 6d shows a 25–50-K increase in  $T_B$ 's on the downshear side of the storm but a decrease on the upshear side, which is consistent with the rotation of convection (e.g., Figs. 5b,c). The convection sampled by the ER-2 during the time period shown in Fig. 6 represents a portion of a convective burst episode similar to that outlined in the IR satellite imagery in Figs. 5a,b.

Figure 7a shows the track of the ER-2 between 1420 and 1432 UTC 9 July on top of the four AMPR channels. The aircraft cut through just to the south (7–8 km) of the estimated storm center [using the method of Willoughby and Chelmow (1982)]. In addition to the 85-GHz ice scattering, the 37-GHz channel (peaking between 5–8 km height) also shows notable  $T_B$  depressions, providing further evidence of large graupel/ice particles in the

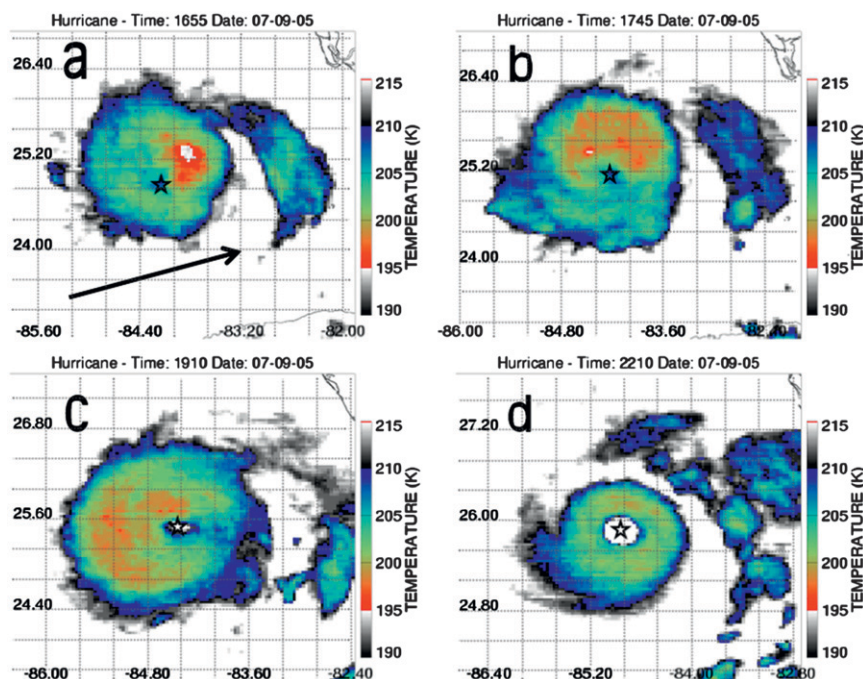


FIG. 5. A series of GOES IR snapshots of Hurricane Dennis in the Gulf of Mexico during one convective burst episode. The times shown on 9 July are (a) 1655, (b) 1745, (c) 1910, and (d) 2210 UTC. The black arrow in (a) denotes the large-scale, storm-relative shear direction valid for this time period. The star represents the estimated storm center. Note that the color scale only goes up to 215 K for visualization purposes. A nearly clear eye was confirmed for (d) with a broader color scale and visible imagery.

convective band to the east of the storm center. To the south of the storm center, the maximum  $T_B$ 's in the 19- and 10-GHz channels, representing low-level (3–5 km) radiation emission by liquid hydrometeors, are closer to the center than the minimum  $T_B$ 's in the 85-GHz channel (southern edge of swath).

Note that Fig. 7a is displayed in scan coordinates so the radiometric signatures will exaggerate the apparent slope of the eyewall. This is clearly evident in a slice of the across-track AMPR data (mapped to the surface) near the TC center in Fig. 7b. There is a  $\sim 7$ -km displacement between the 10-GHz maximum (rainfall) and the 85-GHz minimum (ice). If these channels were mapped to their respective emission–scattering altitudes (see Fig. 7a), then they would be closely aligned. However, the AMPR most likely did not have a wide enough view to see the largest 85-GHz ice scattering on the southern side, which would have shown a displacement in the radiometric signatures and thus a slope in the southern eyewall. The western eyewall also appears to be sloped whereas the eastern eyewall (where the HTs are located, revealed by the 85-GHz scattering) is nearly vertically erect, shown by the collocation of the 85-, 37-, and even some 19-GHz scattering signatures (Fig. 7a).

Figure 8 shows the nadir beam, attenuation-corrected EDOP reflectivity overlaid with the general flow features retrieved from the Doppler velocities along the ER-2 track in Fig. 7a. Between  $\sim 90$  and 105 km along track, hydrometeors are present below 8-km altitude with very few above, which corroborates our interpretation of the passive microwave data. The western or upshear eyewall has relatively weak reflectivities with a clearly defined sloping structure, while the eastern or downshear eyewall is more intense with a vertically erect structure. The high reflectivity in the eastern eyewall is an HT penetrating to nearly 16-km height, having a 30–35-dBZ echo extending to 14-km height and with a width of  $\sim 6$ –8 km.

Figure 9a shows the retrieved vertical velocities along the flight line. Vertical motion as low as 75 m above the ocean surface can be resolved with EDOP, a distinct advantage over other airborne radars. However, in nature, updrafts are 3D and the nonscanning beams of EDOP only allow cross sections of vertical velocity to be analyzed. The western eyewall has pockets of moderate vertical motion ( $5$ – $10 \text{ m s}^{-1}$ ) between  $\sim 6$ - and 14-km height that follow the sloping structure seen in the reflectivity. The eastern eyewall is dominated by strong

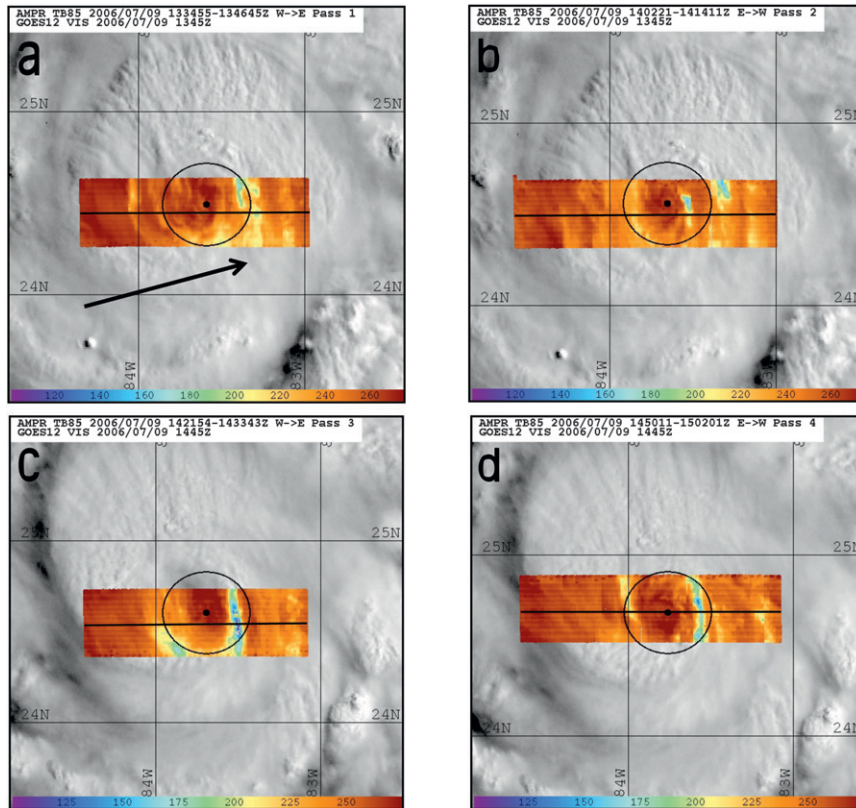


FIG. 6. Twelve-minute flight segments of the AMPR 85-GHz  $T_B$ 's from the four ER-2 overpasses on 9 July 2005, overlaid on the nearest-time GOES-12 visible satellite imagery. The small black dot at the center of each panel represents the estimated storm center using the method of Willoughby and Chelmow (1982), the horizontal line denotes the track of the ER-2, and the circle depicts the mean radius of maximum wind (25 km) during this period. (a) Pass 1 (west to east), 1334–1346 UTC; (b) pass 2 (east to west), 1402–1414 UTC; (c) pass 3 (west to east), 1421–1433 UTC; and (d) pass 4 (east to west), 1450–1502 UTC. The black arrow in (a) denotes the large-scale, storm-relative shear direction valid for this flight period.

updrafts within the HT extending into the boundary layer with maximum vertical velocities of  $20 \text{ m s}^{-1}$  at 13-km altitude. The AMPR  $T_B$  evolution on  $\sim 20$ -min time scales in Fig. 6 indicates that the convective burst observed during this pass may have been close to its peak intensity. However, based on the 85-GHz channel in Fig. 7a, there is small-scale  $T_B$  variability in the eastern eyewall and the EDOP cross section only represents a sample of this convection, which may not reveal the most intense updrafts.

Figure 9b shows a close-up view of the vertical velocity structure within the HT. At 110 km along track there are two main updraft sections with a separation around 6 km height by a  $\sim 5$ – $7 \text{ m s}^{-1}$  downdraft. Uncertainty in mixed phase particle fall speeds in this region ( $\sim 2$ – $3 \text{ m s}^{-1}$ ; Heymsfield et al. 1999, 2010) could change the value of the peak downdraft, but not the sign. Heymsfield et al. (2010) presented 13 peak updrafts in

hurricane deep convection and found similar decreases in updrafts (and increases in downdrafts) at 6-km height. The lower, 3-km-wide updraft section has maximum vertical motion of  $12 \text{ m s}^{-1}$  and is tilting with the eyewall tangential motion. The upper section contains a wider ( $\sim 5 \text{ km}$ ) updraft with velocities increasing with height up to the EDOP-defined cloud top, suggesting the presence of buoyancy powered by the latent heat of freezing (Zipser 2003). Significant downdrafts ( $\sim 3$ – $10 \text{ m s}^{-1}$ ) are present within the HT surrounding the updrafts as would be expected to conserve mass. For example, a strong  $\sim 10 \text{ m s}^{-1}$  downdraft at 114 km along track and at an altitude of 5–6 km could have been enhanced by a combination of cooling and loading of air resulting from melting hydrometeors (Heymsfield et al. 2010). The downdrafts in Fig. 9b may be the start of a broader region of subsidence similar to that observed in Heymsfield et al. (2001).

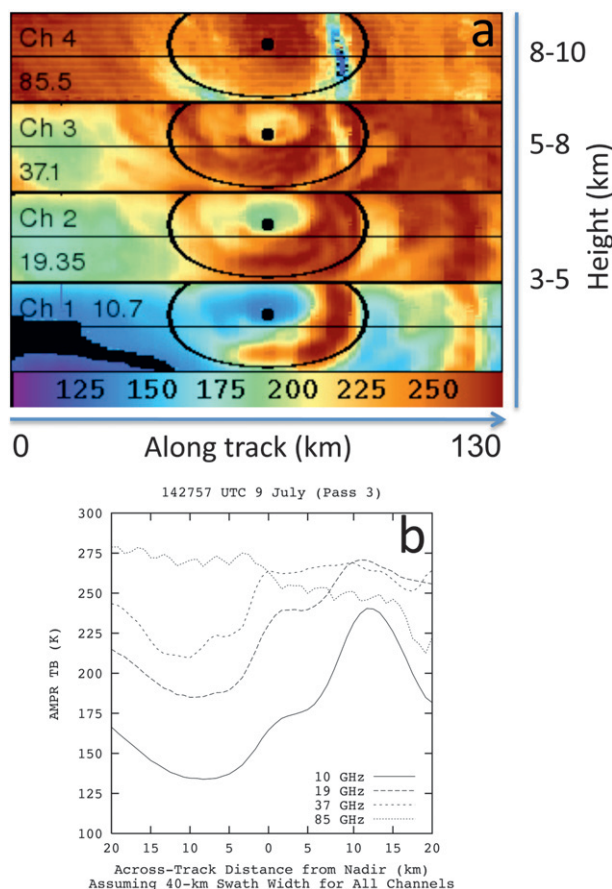


FIG. 7. (a) Zoomed-in view of the AMPR  $T_B$ 's for channels 1 (10 GHz), 2 (19 GHz), 3 (37 GHz), and 4 (85 GHz) during the third ER-2 overpass (Fig. 6c) between 1421 and 1433 UTC 9 July 2005. The thin black line through the center of each swath is the track of the ER-2, the ellipse is the mean RMW (25 km) for this time period, and the dot is the estimated storm center [using the method of Willoughby and Chelmon (1982)]. The approximate heights for each channel (Spencer et al. 1994) and along-track distances are labeled on the figure. Note that the RMW is elliptically shaped, since in AMPR scan coordinates the along-track and across-track pixel resolutions are different. (b) Across-track slice of AMPR  $T_B$ 's from (a) closest to the storm center. All channels are mapped to the surface (40-km swath width). See text for discussion.

The west to east track of the third ER-2 overpass (1420–1432 UTC 9 July) provides a cross section of zonal winds (Fig. 10a), with the storm motion removed, within the eyewall and HT. Although these winds are not radial because the ER-2 did not pass through the TC center (7–8 km off center), they still show common features of the hurricane secondary circulation, which can be quite broad, such as a region of strong ( $\sim 20 \text{ m s}^{-1}$ ) sloping outflow in the western eyewall. The  $10 \text{ m s}^{-1}$  current of air just under the outflow flowing toward the core of the storm appears to be dry, as the reflectivity in this region has been diminished (Fig. 8). Note that the

features in the western eyewall described above can also be seen in the same locations in a pass through the storm center shown later in this section (Fig. 15a). Below  $\sim 8$ -km altitude, EDOP is sampling the zonal component of the eyewall tangential flow with values near  $25 \text{ m s}^{-1}$  as low as 0.5 km (first clutter-free gate in forward beam) above the ocean surface.

Zooming in on the HT, Fig. 10b shows a strong region of converging air from 4- to 10-km altitude meandering through the center of the feature. Above 10-km height, strong diverging air with over  $30 \text{ m s}^{-1}$  of outflow is observed at the top of the HT. Below 4 km,  $15$ – $25 \text{ m s}^{-1}$  flow into the HT from the low-level eyewall may have helped fuel the convective updraft through the transport of entropy-rich air. The EDOP vertical velocities and a reference density profile can be used to compute divergence using the anelastic mass continuity equation ( $\partial u/\partial x + \partial v/\partial y = -\rho^{-1}\partial \rho w/\partial z$ ). Figure 11 shows the divergence field (smoothed with a filter to reduce noise) zoomed in on the HT, revealing convergence structure very similar to the zonal winds shown in Fig. 10b. Maximum values in the filament of convergence at  $\sim 110$ – $114$  km along track and  $\sim 2$ – $12$  km height are on the order of  $10^{-2} \text{ s}^{-1}$ . These ultra-high-resolution observations depict a vigorous transverse circulation in the core of a HT close to its peak intensity.

Approximately 25 min later, the ER-2 crossed over the convective burst region again between 1445 and 1503 UTC 9 July ( $\sim 16.5$  km north of the last pass and  $\sim 0.5$  km north of the storm center at this time), revealing a similar eyewall structure, but with important differences. Figure 12 displays the track of the fourth ER-2 overpass and the storm center overlaid on the four AMPR channels. As noted above, the AMPR data show that convection was decaying on the eastern side of the storm and growing on the western to northwestern portions at this time. Ice particle scattering at 85 and 37 GHz is still present on the eastern side of the storm, but the values have warmed by  $\sim 25$ – $50$  K. In addition, the  $T_B$ 's are more uniform in the eastern eyewall than during the previous overpass (1420–1432 UTC), indicating that the EDOP cross section may be characteristic of a larger portion of the eyewall.

In the western eyewall, the width of the 85-GHz ice scattering is smaller than the previous overpass and only little displacement with the 19-GHz maximum  $T_B$ 's is evident. This indicates that the western eyewall is sloping less than the previous overpass, probably because of the upshear rotation and growth of convection in this region allowing a more vertically oriented structure. The orbital period of air parcels (computed using flight-level data at  $\sim 3.5$ -km height) located where the HTs were observed during the ER-2 overpasses ( $\sim 20$  km) was

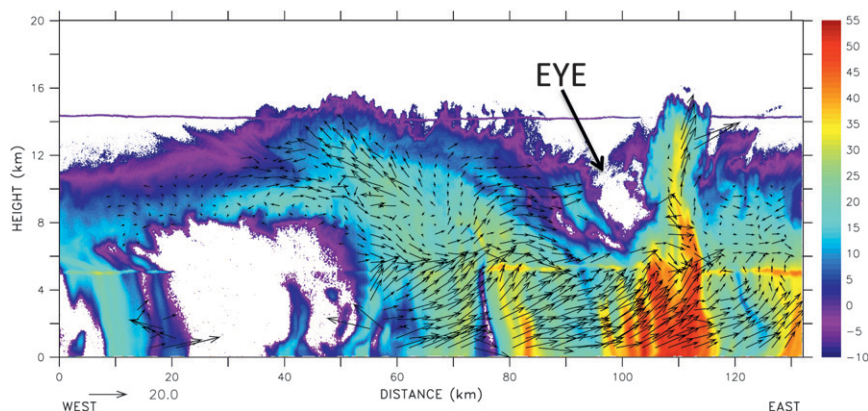


FIG. 8. EDOP attenuation-corrected nadir-beam reflectivity (dBZ) along the track of the ER-2 shown in Fig. 6c between 1420 and 1432 UTC 9 Jul 2005. The wind vectors retrieved from the nadir and forward beams of EDOP are overlaid along with a reference arrow of  $20 \text{ m s}^{-1}$ . Detailed wind plots are provided in subsequent figures. The ER-2 flew from west to east across the eyewall at 20-km altitude. The approximate position of the upper-level eye is marked on the figure.

$\sim 50$  min. Thus, everything else held constant, it would take  $\sim 25$  min for the HTs to reach the western eyewall, which is consistent with the growth of convection in this region (Fig. 6d). The nadir-beam, attenuation-corrected reflectivity at this time (Fig. 13) shows a  $\sim 30$ -dBZ echo extending to 10-km height in a narrow column within the western eyewall ( $\sim 140$  km along track). The reflectivity has decreased (although 20–25-dBZ echoes extend to 14-km height) in the HT slice within the eastern eyewall, which is consistent with the increased 85-GHz  $T_B$ 's shown in Fig. 12. The lack of scatterers between  $\sim 118$  and 131 km along track and below 8 km reveals that the ER-2 tracked through the eye of Dennis, very close to the center of rotation at this time (also shown in the 19–37-GHz image in Fig. 12). Furthermore, the bright band slopes upward toward the storm center, which provides evidence of a building warm core at midlevels (Guimond et al. 2006).

The vertical velocities for this pass (Fig. 14a) reveal a concentrated  $\sim 10 \text{ m s}^{-1}$  updraft peaking at 10-km height and collocated with the high reflectivity region in the western eyewall. This vertical velocity structure is different from that in the last pass (Fig. 9a) where the updrafts were diffuse and sloping outward with height. Zooming in on the HT in the eastern eyewall, Fig. 14b shows a similar structure to the overpass 25 min earlier with two main updraft sections separated at 6-km altitude. As mentioned before, fall speed uncertainties in the melting layer could reverse the sign of the weak downdrafts observed between 100 and 103 km along track and 6-km height. However, a separation of updrafts would still be evident. The upper section appears to be a merger of two individual updrafts into one wide

( $\sim 5$ – $6$  km) and strong (significant region of  $20 \text{ m s}^{-1}$  velocities) feature.

It is stressed here again that the EDOP cross sections only represent a slice through the HT and in reality the updraft has a 3D structure. Therefore, the origination point for the strong updraft at upper levels may not be located directly below this feature. Nevertheless, the two cross sections in Figs. 9b and 14b are similar in their updraft structure, indicating that strong regions of upward motion separated at the melting layer may be characteristic of the HTs in Dennis at this time. In fact, this feature is characteristic of many more HTs than just the ones described here. As mentioned above, Heymsfield et al. (2010) find a very similar updraft minimum at 6-km altitude in their mean profile (13 cases) of deep convection in hurricanes. They attribute this feature to drag from hydrometeor loading just above the freezing level.

The downdrafts in Fig. 14b are more developed than those in the last pass with stronger (peak of  $-12 \text{ m s}^{-1}$ ) and wider (4–6 km) regions of descent flanking the main updraft at upper levels. These observations, along with the AMPR data and EDOP reflectivity, reveal that the HTs in the eastern eyewall of Dennis were beginning to decay during this overpass. We believe that the intense, wide region of descent on the inner edge of the HT in Fig. 14b is similar to the subsidence observed by Heymsfield et al. (2001) in Hurricane Bonnie (1998). The AMPR 85-GHz data (Figs. 6d and 12) show a fairly uniform low- $T_B$  field across track, suggesting that the structure observed by EDOP in the eastern eyewall (i.e., Fig. 13) may be operating in a larger portion of the eyewall. The cumulative effects of descent along the

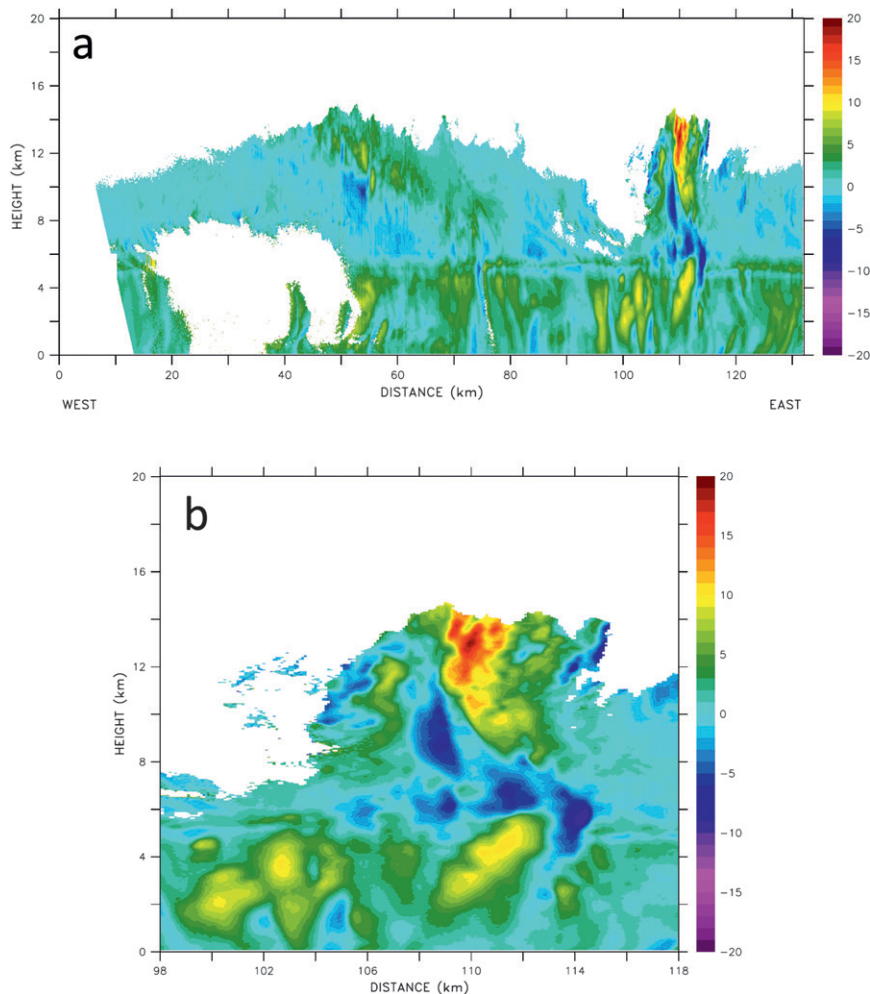


FIG. 9. Retrieved vertical velocities ( $\text{m s}^{-1}$ ) from EDOP within the cross section in Fig. 8 (a) for the entire overpass and (b) zoomed in on the hot tower in the eastern eyewall. Note that the first level of useful data is 75 m above the ocean surface.

inner edge of HTs embedded in the eyewall can produce significant drying and warming (up to  $3^{\circ}\text{C}$ ; Heymsfield et al. 2001) of the eye. The development of a clear eye (Figs. 5c,d) and increases in the warm core (Fig. 4) are likely due to the HT-induced subsidence described above.

Since the ER-2 crossed very close ( $\sim 0.5$  km) to the estimated storm center during the fourth (1445–1503 UTC) overpass, the storm-relative zonal winds along the east to west track in Fig. 15a very nearly represent radial flow into or out of the system center. Note that the 0.5-km off-center displacement is well within the uncertainty of the storm center estimates (3 km; Willoughby and Chelmon 1982). Similar storm center estimates (and uncertainties) have been used in other studies to deduce the radial flow in TCs (e.g., Jorgensen 1984; Marks et al. 2008).

In the western eyewall, the deep (8 km to cloud top), intense ( $20\text{--}25 \text{ m s}^{-1}$ ) region of outflow is similar to the third (1420–1432 UTC) overpass, including the thin region of inflow embedded in the outflow layer. Below 8 km and most pronounced at 3–4-km height, inflow is observed in the western eyewall, which is a common feature of TCs (e.g., Jorgensen 1984). Figure 15b zooms in on the HT and reveals vigorous converging air near 103 km along track and between 8- and 15-km height, with a strong region of diverging air outside of the convergent region between 12 km and the cloud top. Figure 16 shows a zoomed image of the divergence field in the HT, revealing more disorganized structure as compared to Fig. 11, but with similar values. Most of the convergence is located above 6-km height with a strong region of divergence near the cloud top, which is consistent with Fig. 15b.

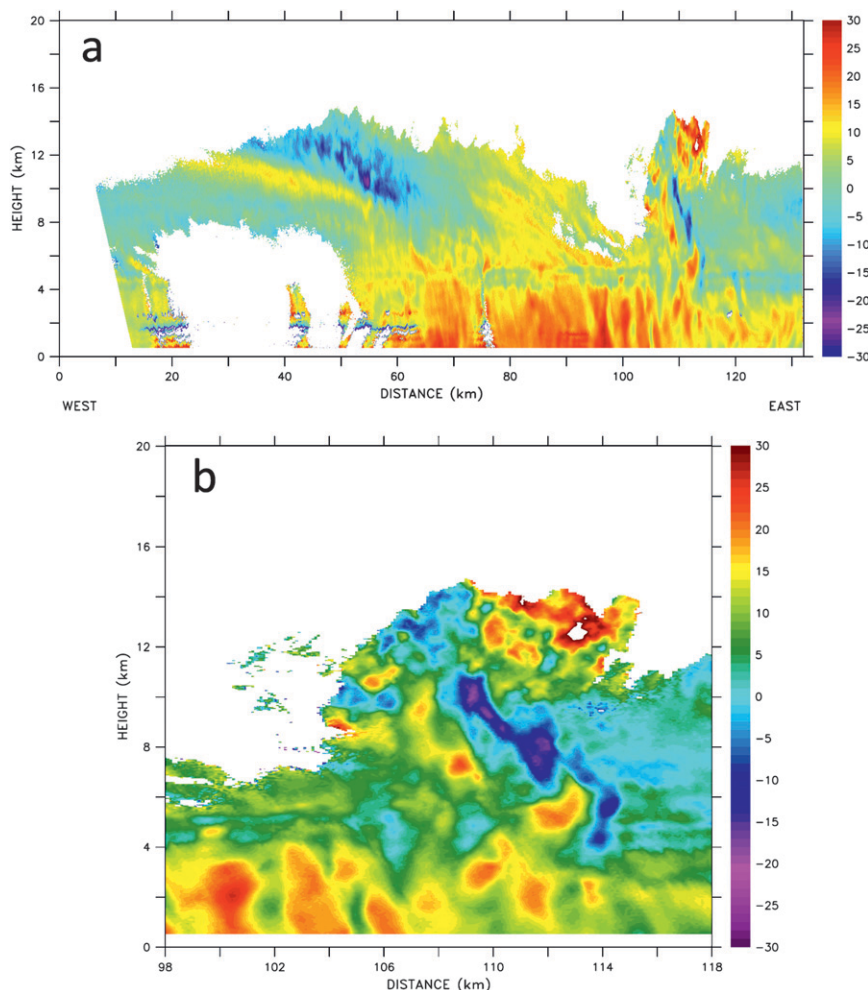


FIG. 10. As in Fig. 9, but for storm-relative zonal winds ( $\text{m s}^{-1}$ ). Note the first level of useful data is 0.5 km above the ocean surface.

As in the third (1420–1432 UTC) overpass, the HT slice at this time has a well-defined transverse circulation in the core of the feature. Outside of the HT core (Figs. 15a,b), the eastern eyewall is dominated by intense inflow ( $15\text{--}20 \text{ m s}^{-1}$ ) extending from  $\sim 10\text{-km}$  altitude down to 0.5 km above the ocean surface and at the eye–eyewall interface (the scatter-free eye is labeled in Fig. 14b for reference). This structure is significantly different from the general inflow found in mature hurricanes (such as that in the western eyewall of Fig. 15a; Jorgensen 1984; Marks and Houze 1987). Implications of these observations are discussed in the next section.

### 5. Effects on the vortex-scale dynamics

Now that we have shown the new remote sensing observations of HTs in the eyewall of a borderline category-2 storm, the question becomes: What are the essential

physics responsible for the rapid intensification of Hurricane Dennis and what is the role of the HTs in this process? In this section, we briefly explore the impact of the HTs on the organization of the warm core and the parent vortex using AMSU satellite and flight-level wind data, respectively.

The GOES IR imagery and high-resolution AMPR and EDOP data shown in the previous section clearly reveal an asymmetric, vertically oriented distribution of convection in the downshear to downshear left portions of the storm for much of 9 July. In contrast, a sloping eyewall structure is observed by AMPR (Figs. 7 and 12) and EDOP (in terms of reflectivity and circulation; Figs. 8 and 13), mainly on the upshear sides of the storm. These microphysical and kinematic observations imply that during the ER-2 overpass periods, the eyewall of Dennis was composed of a superposition of modes including (i) an axisymmetric mode (characterized by an eyewall

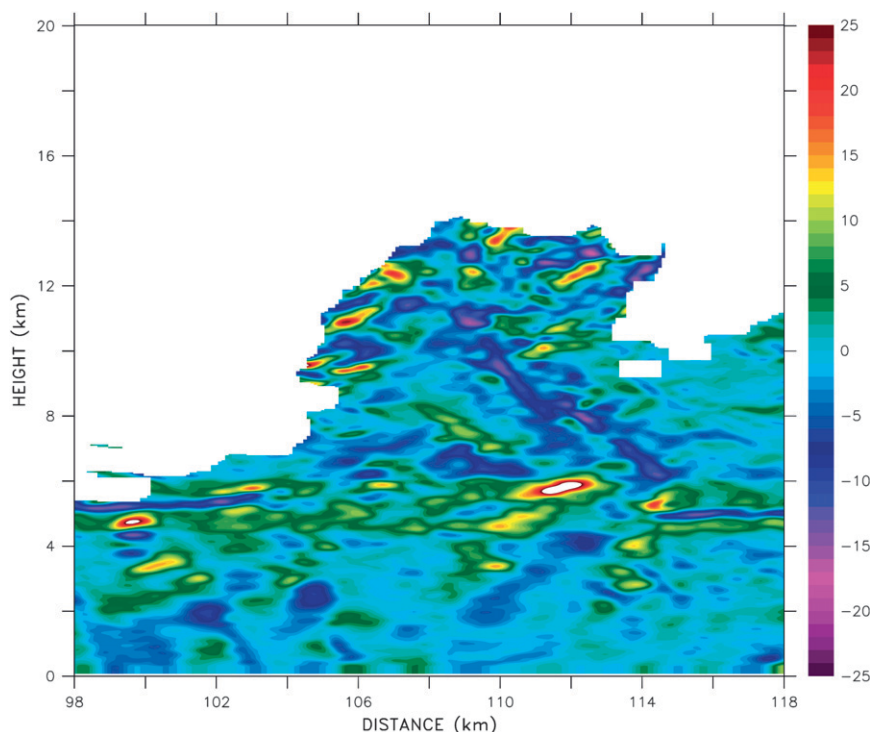


FIG. 11. Divergence ( $\times 10^3 \text{ s}^{-1}$ ) computed using the anelastic mass continuity equation ( $\partial u/\partial x + \partial v/\partial y = -\rho^{-1} \partial \rho w/\partial z$ ) for the same time period and location as Fig. 10b. Note that the horizontal lines of convergence–divergence outside of the HT core ( $\sim 105$ – $114$  km along track) and at 5–6-km height are noise from the bright band. Values have been smoothed with a filter to reduce noise.

possibly neutral to slantwise moist ascent; Emanuel 1986) shown by the sloping structure on the upshear sides of the storm and (ii) an asymmetric mode with the potential for significant local buoyancy to vertical displacements shown by the HTs in the downshear eyewall (Braun 2002).

Based on animation of GOES IR imagery and Fig. 5, the asymmetric mode was active from the time Dennis emerged into the Gulf of Mexico (0900 UTC 9 July) until roughly 2210 UTC 9 July (Fig. 5d) when the IR  $T_{BS}$  in the inner core became strongly axisymmetric. To illustrate the contribution of the asymmetric mode in Dennis' warm core, all AMSU overpasses (stars in Fig. 3a) were first interpolated to a cylindrical grid extending from the NHC storm center out to 600-km radius. The temperature anomalies were then Fourier decomposed in azimuth and the contribution of the asymmetric portion relative to the total (defined as the ratio  $\beta$ ) was computed as

$$\beta(r, z) = \frac{\sum_{i=1}^{\infty} \lambda_i(r, z)}{\sum_{i=0}^{\infty} \lambda_i(r, z)}, \quad (1)$$

where  $\lambda_i$  represents a specific azimuthal wavenumber of the temperature anomalies (hereafter warm core) as a function of radius  $r$  and height  $z$ . In computing the asymmetric and total components, the summations were truncated at wavenumber 10. Figure 17 displays  $\beta$  for the

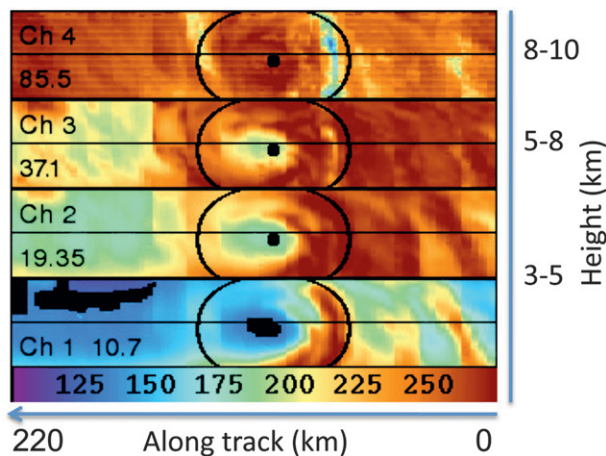


FIG. 12. As in Fig. 7a, but for the fourth ER-2 overpass (Fig. 6d) between 1450 and 1502 UTC 9 Jul 2005.

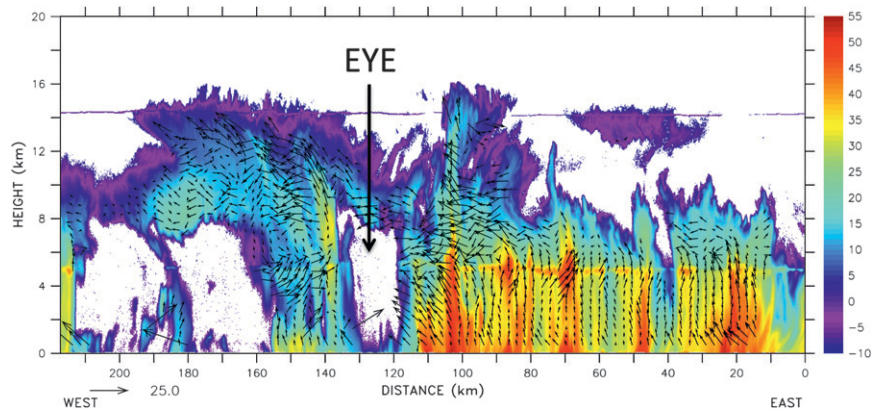


FIG. 13. As in Fig. 8, but along the track of the ER-2 shown in Fig. 6d between 1445 and 1503 UTC 9 Jul 2005. The ER-2 flew from east to west very close to the center of rotation at this time.

life cycle of Dennis between 50- and 600-km radius from the storm center and averaged over the 300–150-hPa layer. We compute ratios in (1) to avoid the biases introduced by time-varying footprint resolutions (see sec-

tion 3). The structure shown in Fig. 17 was tested for sensitivity to the estimated storm centers by perturbing the track 10–25 km in all four cardinal directions. The results revealed that Fig. 17 is not sensitive to the location

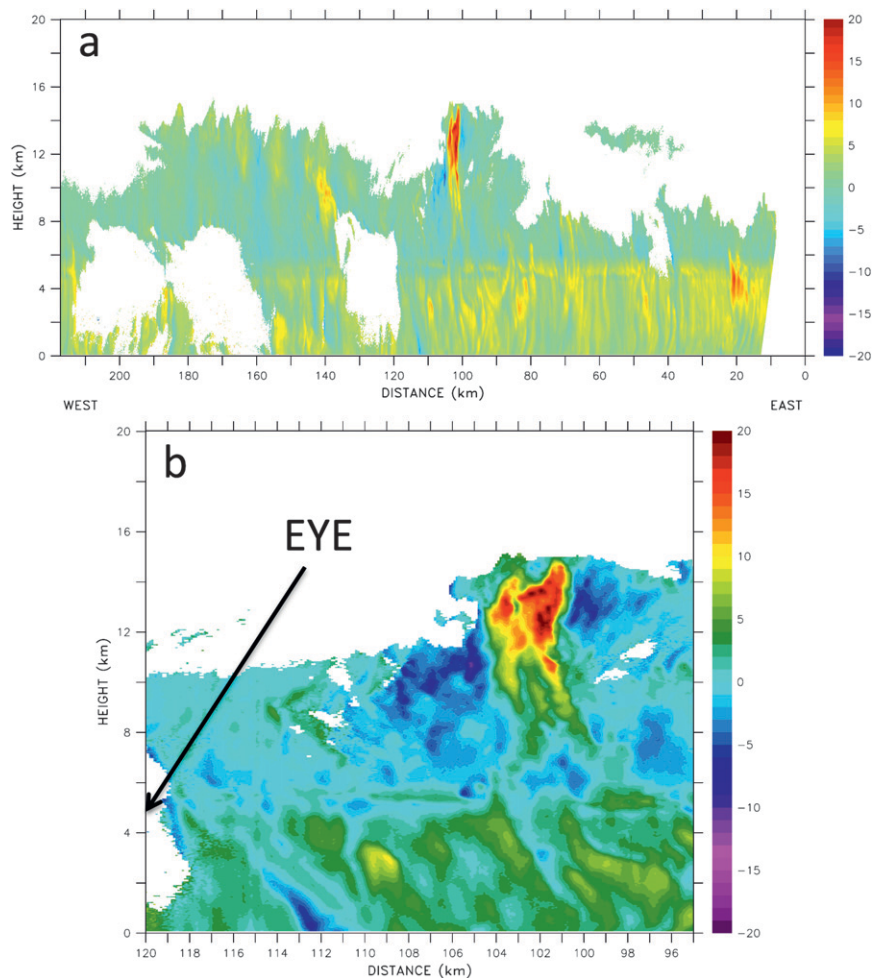


FIG. 14. As in Fig. 9, but within the cross section in Fig. 13.

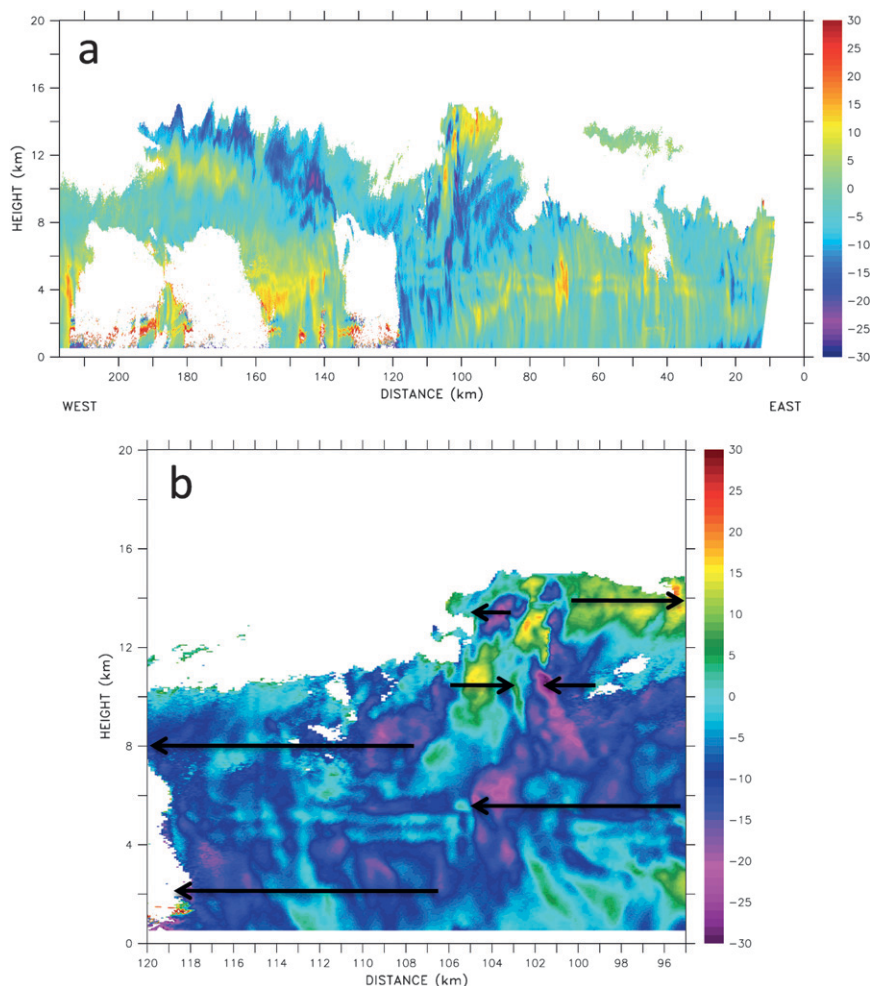


FIG. 15. As in Fig. 14, but for storm-relative radial winds ( $\text{m s}^{-1}$ ). The arrows in (b) depict the general flow features in the hot tower and eyewall. The position of the eye is marked in Fig. 14b. Note that the first level of useful data is 0.5 km above the ocean surface.

of the system center. Note that a smooth time series is produced by linearly interpolating between the AMSU overpasses.

The asymmetric contribution to the warm core of Dennis is large (40%–50% at 50 km radius) between 0000 and 0600 UTC 9 July mainly because of landfall in Cuba, although the storm was embedded within an environment of weak vertical wind shear (mean value of  $\sim 6 \text{ m s}^{-1}$ ). Around 1800 UTC 9 July and extending into 10 July, the asymmetric contribution drops by  $\sim 20\%$  from 50- to 250-km radius, revealing a large-scale transition of the warm core to a more axisymmetric structure. Spatial plots of the warm core (not shown) verify the axisymmetric transition observed in Fig. 17, which is consistent with Fig. 5 and the IR satellite animation.

We hypothesize that the growth (Fig. 4 and section 3) and axisymmetric transition (Fig. 17) of Dennis' warm

core was due to the outbreak of HTs (and overall deep convection) and the vortex Rossby wave dynamics that comprise the axisymmetrization process (see discussion in introduction; Montgomery and Kallenbach 1997; Montgomery and Enagonio 1998). The Doppler radar observations presented here show that subsidence on the inner edge of the HTs and its transport toward the eye were significant. As the HTs ignite on the downshear side of the storm, their rotation upshear stimulates regions of strong vertical motion (see orbital period discussion in section 4 and Fig. 14a, western eyewall) and attendant subsidence. This cyclonically wrapped subsidence warms and dries the eye in an axisymmetric fashion. The development of subsidence that projects onto wavenumber zero and its relationship to intensifying the warm core is similar to the idealized study of Montgomery and Enagonio (1998).

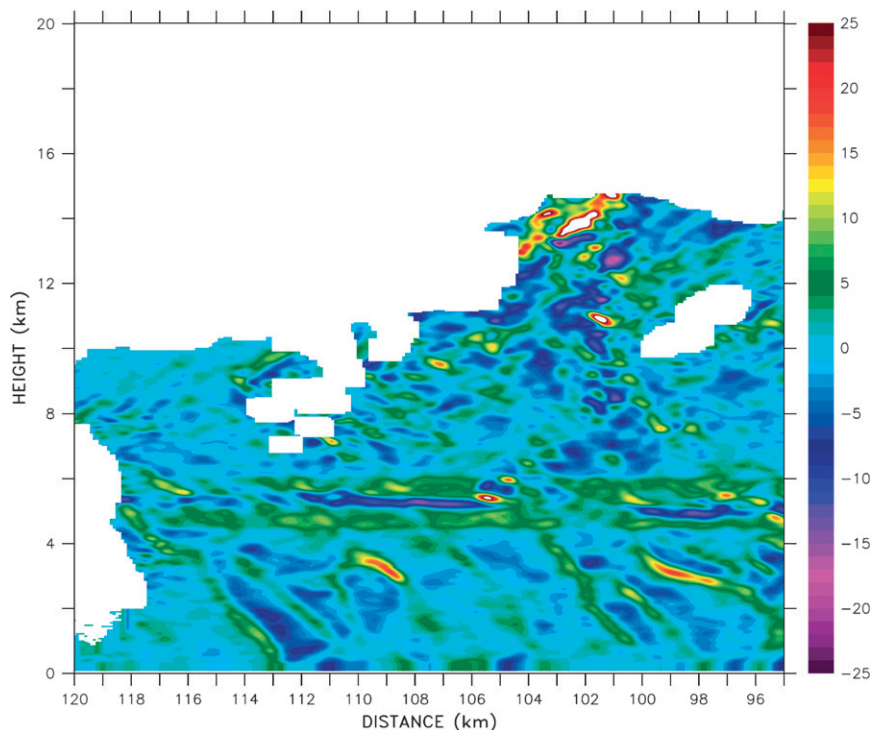


FIG. 16. As in Fig. 11, but for the time period in Fig. 13 and location described in Fig. 15b. Note that the bright band is more evident in this pass, shown by the horizontal lines of convergence–divergence at 5–6-km height through most of the along-track distance.

The HTs (and overall deep convection) not only had an effect on the thermodynamics of the vortex, they also influenced the inner core dynamics examined here using flight-level wind measurements. Figure 18 shows the tangential winds for all “passes” (average of inbound and outbound flight legs) through the center of Dennis between  $\sim 3$ - and 3.6-km height. The tangential wind profile after Dennis emerged into the Gulf of Mexico was rather flat (i.e., no clear peak) with maximum tangential winds of  $30\text{--}35\text{ m s}^{-1}$ . However, just after the ER-2 flights (HTs located at  $\sim 20$ -km radius), a peaked profile was evident with the RMW contracting from  $\sim 20$  to 10 km and the maximum winds increasing to  $60\text{ m s}^{-1}$  in 15 h.

Axisymmetric, balanced theory shows that one effect of HTs on a TC is through modification of the vortex-scale inertial stability and a concurrent increase in the efficiency of the storm (Shapiro and Willoughby 1982; Schubert and Hack 1982; Hack and Schubert 1986; Nolan et al. 2007). The axisymmetric, relative inertial stability ( $\bar{I}^2$ ) can be represented as

$$\bar{I}^2 = \left( \frac{\partial r \bar{v}}{r \partial r} \right) \left( \frac{2 \bar{v}}{r} \right), \quad (2)$$

where  $v$  is tangential wind,  $r$  is the radius from the TC center, and the overbar indicates an azimuthal mean. As discussed in section 1, HTs add a large source of vertical vorticity<sup>1</sup> (Reasor et al. 2005; Montgomery et al. 2006; Houze et al. 2009) or tangential wind into the background vortex that increases  $\bar{I}^2$  and leads to stronger resistance to parcel displacement in the radial direction. Increased resistance allows for greater efficiency in the dynamic response to imposed sources of convective heating (i.e., HTs). Thermal efficiency is defined as the ratio of *net* heating (convective heating plus adiabatic cooling) to convective heating with the hydrostatic response to the net heating producing lowered surface pressures and stronger tangential flow (Schubert and Hack 1982). Net heating can also occur as a result of subsidence when adiabatic warming outweighs the effects of convective cooling. The thermal efficiency arguments of Schubert and Hack (1982) and the recent results of Schubert et al. (2007) imply that the inertial

<sup>1</sup> Although the vertical component of vorticity cannot be computed with EDOP, information on the stretching of pre-existing vorticity (combining flight-level winds and EDOP) can be determined and was found to be consistent with previous studies (i.e., Montgomery et al. 2006).

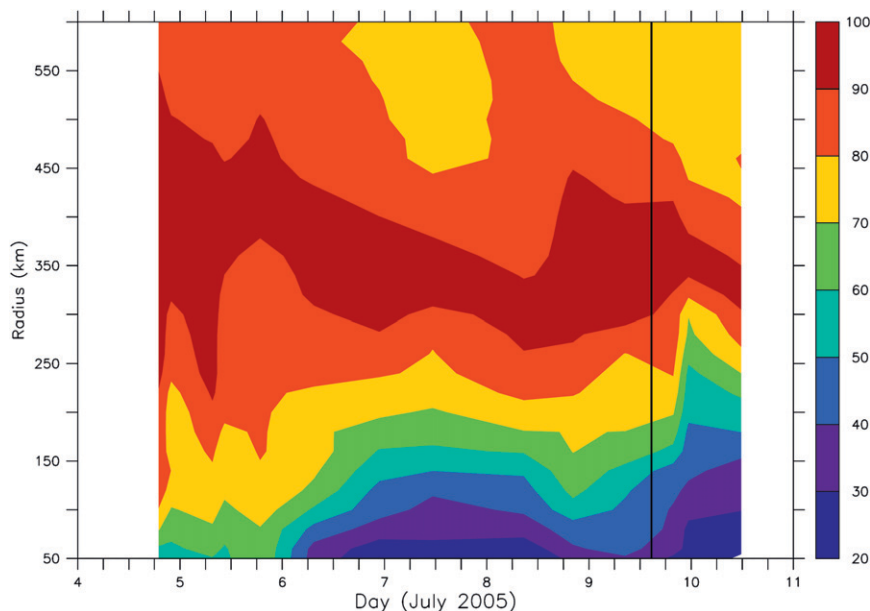


FIG. 17. Contribution (%) of the asymmetric part of the temperature anomalies (or warm core) to the total temperature anomalies computed according to (1) and averaged over the 300–150-hPa layer for the life cycle of Dennis. The thick black line is as in Fig. 3.

stability of the storm should evolve in a coupled fashion with the warm core. It should be noted that the inertial stability framework for vortex intensification discussed above can also be thought of in terms of vorticity, where HTs stretch pre-existing vorticity locally, leading to changes in the symmetric part of the mass (warm core) and momentum (tangential wind) field to maintain thermal wind balance.

The aircraft passes and their azimuthal coverage over a certain time period provide an effective measure of the axisymmetric part of the flow valid as an average over the time interval chosen (similar to Mallen et al. 2005). Figure 19 shows axisymmetric tangential wind and inertial stability profiles from flight-level data averaged for a 12-h period before (8 passes) and after (13 passes) the ER-2 HT observations. In the 12 h following the ER-2 flights, the axisymmetric tangential wind profile developed a distinct peak at  $\sim 15$ -km radius with a  $15 \text{ m s}^{-1}$  increase in maximum winds from the previous period. In addition, from 5- to 25-km radius, the axisymmetric profile of inertial stability increased with the largest enhancements (by a factor of nearly 3) occurring at the approximate radius where the HTs were observed (15–20 km). Changes to the time interval chosen for comparison (12 h) did not alter the qualitative structure. The increase in inertial stability in the 12 h after the ER-2 observations would allow for greater net heating in the core (Fig. 4 and section 3), including possibly both the upward and downward branches of the HT transverse circulations.

## 6. Summary and conclusions

In this paper, we have shown new and unique airborne Doppler radar and passive microwave observations of HTs occurring in Hurricane Dennis (2005) just before a period of rapid intensification (11-hPa pressure drop in 1 h 35 min) during the NASA TCSP experiment. The beam geometry of EDOP provides for some of the finest-resolution and lowest-uncertainty (direct measurement of vertical component of Doppler velocity) wind retrievals of any current airborne radar. In addition, we have examined the potential impact of the HTs on the organization and growth of the warm core, including the coupling to the inner-core dynamics using satellite and aircraft flight-level measurements.

After Dennis emerged off of Cuba and into the Gulf of Mexico as a borderline category-2 storm, IR imagery revealed a  $\sim 12$ -h period of episodic convective bursts in its downshear to downshear left portions. The bursts went through a period of initiation–growth in the downshear quadrants and rotation–dissipation in the upshear quadrants. At the end of the 12-h period (near 2210 UTC 9 July), the convective cloud field displayed a remarkable axisymmetric structure with a clear eye and falling surface pressure.

As part of the TCSP experiment, the NASA ER-2 aircraft made four nearly coincident overpasses of the storm during one convective burst episode on 9 July 2005. Two of these passes, separated by  $\sim 25$  min and

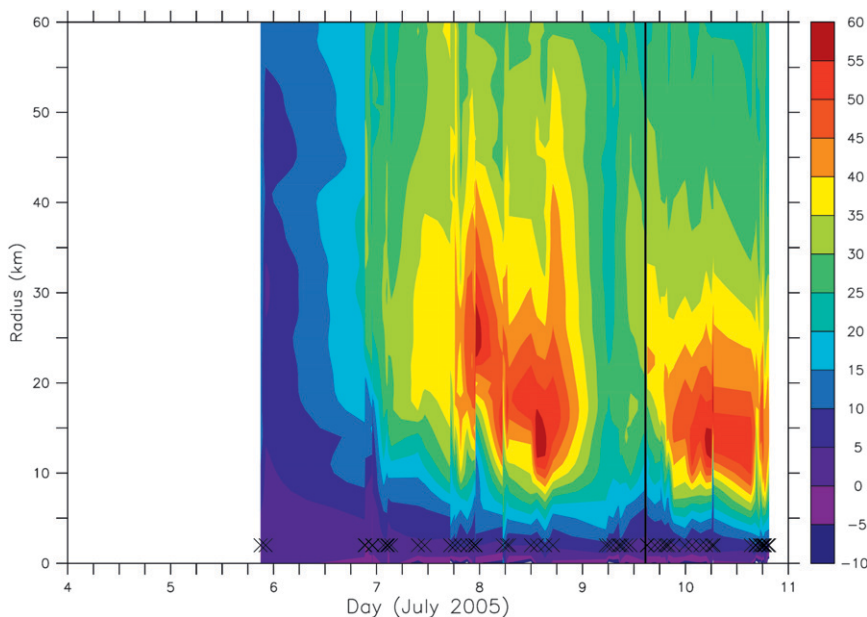


FIG. 18. Time series of inner-core, flight-level tangential winds ( $\text{m s}^{-1}$ ) for all “passes” (average of inbound and outbound flight legs) through the center of Dennis between  $\sim 3$ - and  $3.6$ -km height. The  $\times$ 's mark the times corresponding to the center of each pass (74 total). The black line is the same as in Fig. 3.

16.5 km, revealed 16-km-deep HTs in the downshear (eastern) eyewall, large 85- and 37-GHz ice scattering, and vigorous transverse circulations through the cloud cores. In the plane of the cross sections, the transverse

circulations consisted of deep inflow, maximum updrafts of  $20 \text{ m s}^{-1}$  between 12- and 14-km altitude, and strong outflow near the cloud top. In addition, downdrafts of  $10$ – $12 \text{ m s}^{-1}$  flanking the main updraft were also

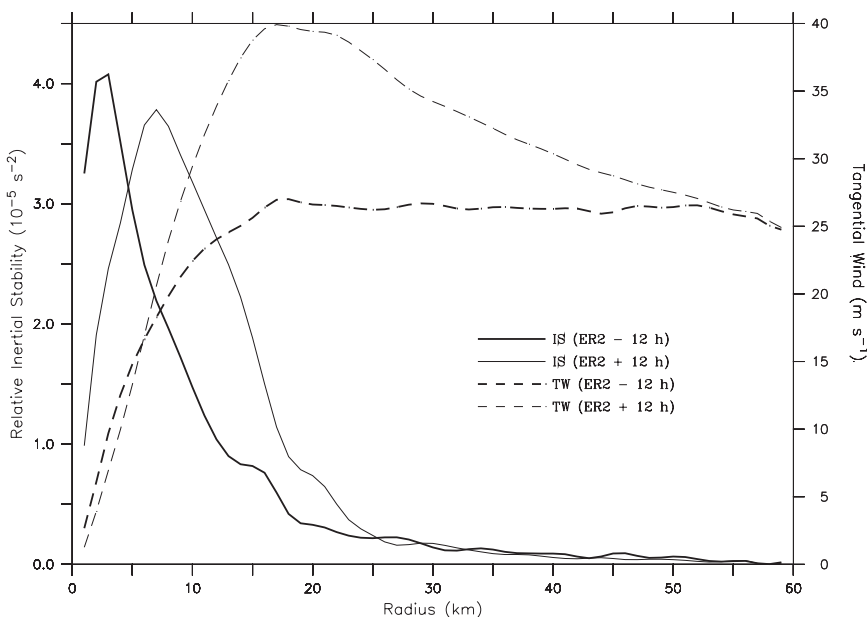


FIG. 19. Flight-level symmetric tangential wind (TW) profiles averaged for a 12-h period before (8 passes) and after (13 passes) the ER-2 hot tower observations, along with the corresponding profiles of relative inertial stability (IS) computed according to (2). See text for details on the calculations.

observed, especially during the fourth overpass (Fig. 14b) when the convection had begun to decay. This subsidence was transported toward the eye by  $15\text{--}20\text{ m s}^{-1}$  inflow occurring over a deep layer ( $0.5\text{--}10\text{ km}$ ) extending from the HT core ( $20\text{-km}$  radius) to the eye–eyewall interface. Strong radial inflow at the eye–eyewall interface has important implications for storm intensification through the radial flux of angular momentum into the eye (Shapiro and Willoughby 1982; Emanuel 1997).

The large-scale warm core of Dennis was shown to transition from an asymmetric to more axisymmetric structure, consistent with the IR imagery,  $7\text{--}8\text{ h}$  after the ER-2 HT observations and  $\sim 12\text{ h}$  after the storm emerged into the Gulf of Mexico and the convective bursts began. In addition, the magnitude of the warm core was observed to increase by  $1.5\text{--}2.0\text{ K}$  during and just after this time period. We attribute this large-scale transition of the warm core to the axisymmetrization process and the convectively induced downdrafts on the inner edge of the eyewall. Using EDOP data, Heymsfield et al. (2001) also observed a broad, strong subsidence region on the inner edge of an HT in Hurricane Bonnie (1998) during the end of an intensification cycle. They estimated that up to  $3^\circ\text{C}$  of eye warming resulted from one or more of the convectively induced downdrafts, within the range of growth shown in this paper ( $\sim 2\text{ K}$ ).

The nature of the dynamic processes in the TC core depends crucially on the HT (and overall deep convection) characteristics and the background vortex in which they exist. The time-mean inertial stability, computed from flight-level wind measurements, was shown to increase by almost a factor of 3 in the  $12\text{ h}$  after the ER-2 overpasses (relative to the previous  $12\text{ h}$ ) near the radii where the HTs were observed. By adding large sources of vorticity into the background flow, we hypothesize that the HTs generated a dynamically protected inner core allowing for more efficient development, including strong subsidence that would lead to a warming of the eye (Schubert and Hack 1982; Schubert et al. 2007).

The grand scope of the observations and analyses shown in this paper suggests that the convective burst with embedded HTs played an important role in driving Dennis into an intense state. These unique observations raised many interesting questions and clearly more research needs to be done to understand the role of HTs (and weaker, more frequent deep convection) and their symmetric and asymmetric components in the intensification process. Specifically, we are interested in a deeper understanding of the scales of motion captured by EDOP and their feedbacks to the system scale. Observationally forced simulations (with P-3 and EDOP data) along these lines are currently being conducted. New remote sensing instruments as well as additional

field experiments will undoubtedly help the community continue to answer many important questions on the science of hurricane intensification.

**Acknowledgments.** Much of this work was completed while the first author was an intern at the Naval Research Laboratory (NRL) in Monterey, CA, through the Naval Research Enterprise Internship Program (NREIP). Thanks go out to John Knaff of the Cooperative Institute for Research in the Atmosphere (CIRA) for providing and assisting with the AMSU data. We thank Dr. Steven Miller and Mr. Jeff Hawkins of NRL Monterey for many discussions throughout the project. In addition, excellent comments from Paul Reasor, Pat Harr, Chris Velden, Mike Montgomery, and two anonymous reviewers are acknowledged. This research was supported by the NASA TCSP experiment and the NASA Ocean Vector Wind Science Team.

## REFERENCES

- Aberson, S. D., M. L. Black, R. A. Black, R. W. Burpee, J. J. Cione, C. W. Landsea, and F. D. Marks Jr., 2006: Thirty years of tropical cyclone research with the NOAA P-3 aircraft. *Bull. Amer. Meteor. Soc.*, **87**, 1039–1055.
- Beven, J., 2005: Tropical cyclone report: Hurricane Dennis 4–13 July 2005. National Hurricane Center, 24 pp. [Available online at <http://www.nhc.noaa.gov/2005atlan.shtml>.]
- Black, M. L., R. W. Burpee, and F. D. Marks Jr., 1996: Vertical motion characteristics of tropical cyclones determined with airborne Doppler radial velocities. *J. Atmos. Sci.*, **53**, 1887–1909.
- Braun, S. A., 2002: A cloud-resolving simulation of Hurricane Bob (1991): Storm structure and eyewall buoyancy. *Mon. Wea. Rev.*, **130**, 1573–1592.
- , M. T. Montgomery, and Z. Pu, 2006: High-resolution simulation of Hurricane Bonnie (1998). Part I: The organization of eyewall vertical motion. *J. Atmos. Sci.*, **63**, 19–42.
- Brueske, K. F., and C. S. Velden, 2003: Satellite-based tropical cyclone intensity estimation using the NOAA-KLM series Advanced Microwave Sounding Unit (AMSU). *Mon. Wea. Rev.*, **131**, 687–697.
- Cecil, D. J., and E. J. Zipser, 1999: Relationships between tropical cyclone intensity and satellite-based indicators of inner core convection: 85-GHz ice-scattering signature and lightning. *Mon. Wea. Rev.*, **127**, 103–123.
- Corbosiero, K. L., and J. Molinari, 2002: The effects of vertical wind shear on the distribution of convection in tropical cyclones. *Mon. Wea. Rev.*, **130**, 2110–2123.
- DeMaria, M., and J. Kaplan, 1994: Sea surface temperature and the maximum intensity of Atlantic tropical cyclones. *J. Climate*, **7**, 1324–1334.
- Demuth, J. L., M. DeMaria, J. A. Knaff, and T. H. Vonder Haar, 2004: Evaluation of Advanced Microwave Sounding Unit tropical cyclone intensity and size estimation algorithms. *J. Appl. Meteor.*, **43**, 282–296.
- Eliassen, A., 1951: Slow thermally or frictionally controlled meridional circulation in a circular vortex. *Astrophys. Norv.*, **5**, 19–60.
- Emanuel, K. A., 1986: An air–sea interaction theory for tropical cyclones. Part I: Steady-state maintenance. *J. Atmos. Sci.*, **43**, 585–605.

- , 1997: Some aspects of hurricane inner-core dynamics and energetics. *J. Atmos. Sci.*, **54**, 1014–1026.
- Frank, W. M., and E. A. Ritchie, 2001: Effects of vertical wind shear on the intensity and structure of numerically simulated hurricanes. *Mon. Wea. Rev.*, **129**, 2249–2269.
- Gamache, J. F., F. D. Marks Jr., and F. Roux, 1995: Comparison of three airborne Doppler sampling techniques with airborne in situ wind observations in Hurricane Gustav (1990). *J. Atmos. Oceanic Technol.*, **12**, 171–181.
- Gentry, R. C., T. T. Fujita, and R. C. Sheets, 1970: Aircraft, spacecraft, satellite, and radar observations of Hurricane Gladys, 1968. *J. Appl. Meteor.*, **9**, 837–850.
- Goldberg, M. D., 1999: Generation of retrieval products from AMSU-A: Methodology and validation. *Proc. 10th Int. TOVS Study Conf.*, Boulder, CO, Bureau of Meteorological Research Centre, 215–229.
- , D. S. Crosby, and L. Zhou, 2001: The limb adjustment of AMSU-A observations: Methodology and validation. *J. Appl. Meteor.*, **40**, 70–83.
- Guimond, S. R., 2007: A diagnostic study of the effects of trough interactions on tropical cyclone QPF. M.S. thesis, Dept. of Meteorology, The Florida State University, 57 pp.
- , F. J. Turk, C. B. Blankenship, and J. D. Hawkins, 2006: Detecting tropical cyclone structural change with the TRMM Precipitation Radar (PR) and Advanced Microwave Sounding Unit (AMSU). Preprints, *27th Conf. on Hurricanes and Tropical Meteorology*, Atlanta, GA, Amer. Meteor. Soc., 6A.2. [Available online at <http://ams.confex.com/ams/pdfpapers/103215.pdf>.]
- Hack, J. J., and W. H. Schubert, 1986: Nonlinear response of atmospheric vortices to heating by organized cumulus convection. *J. Atmos. Sci.*, **43**, 1559–1573.
- Halverson, J., and Coauthors, 2007: NASA's Tropical Cloud Systems and Processes experiment: Investigating tropical cyclogenesis and hurricane intensity change. *Bull. Amer. Meteor. Soc.*, **88**, 867–882.
- Hawkins, J. D., M. Helveston, T. F. Lee, F. J. Turk, K. Richardson, C. Sampson, J. Kent, and R. Wade, 2006: Tropical cyclone multiple eyewall configurations. Preprints, *27th Conf. on Hurricanes and Tropical Meteorology*, Amer. Meteor. Soc., Monterey, CA, 6B.1. [Available online at <http://ams.confex.com/ams/pdfpapers/108864.pdf>.]
- Hendricks, E. A., M. T. Montgomery, and C. A. Davis, 2004: On the role of “vortical” hot towers in the formation of Tropical Cyclone Diana (1984). *J. Atmos. Sci.*, **61**, 1209–1232.
- Heysfield, G. M., and Coauthors, 1996: The EDOP radar system on the high-altitude NASA ER-2 aircraft. *J. Atmos. Oceanic Technol.*, **13**, 795–809.
- , J. B. Halverson, and I. J. Caylor, 1999: A wintertime Gulf Coast squall line observed by EDOP airborne Doppler radar. *Mon. Wea. Rev.*, **127**, 2928–2950.
- , —, J. Simpson, L. Tian, and T. P. Bui, 2001: ER-2 Doppler radar investigations of the eyewall of Hurricane Bonnie during the Convection and Moisture Experiment-3. *J. Appl. Meteor.*, **40**, 1310–1330.
- , L. Tian, A. J. Heysfield, L. Li, and S. Guimond, 2010: Characteristics of deep tropical and subtropical convection from nadir-viewing high-altitude airborne Doppler radar. *J. Atmos. Sci.*, **67**, 285–308.
- Hildebrand, P. H., and Coauthors, 1996: The ELDORA/ASTRAIA airborne Doppler weather radar: High-resolution observations from TOGA COARE. *Bull. Amer. Meteor. Soc.*, **77**, 213–232.
- Hood, R. E., and Coauthors, 2006: Classification of tropical oceanic precipitation using high-altitude aircraft microwave and electric field measurements. *J. Atmos. Sci.*, **63**, 218–233.
- Houze, R. A., Jr., and Coauthors, 2006: The Hurricane Rainband and Intensity Change Experiment: Observations and modeling of Hurricanes Katrina, Ophelia, and Rita. *Bull. Amer. Meteor. Soc.*, **87**, 1503–1521.
- , W. C. Lee, and M. M. Bell, 2009: Convective contribution to the genesis of Hurricane Ophelia (2005). *Mon. Wea. Rev.*, **137**, 2778–2800.
- Iguchi, T., and R. Meneghini, 1994: Intercomparison of single-frequency methods for retrieving a vertical rain profile from airborne or spaceborne radar data. *J. Atmos. Oceanic Technol.*, **11**, 1507–1516.
- Jones, T. A., D. Cecil, and M. DeMaria, 2006: Passive-microwave-enhanced statistical hurricane intensity prediction scheme. *Wea. Forecasting*, **21**, 613–635.
- Jorgensen, D. P., 1984: Mesoscale and convective-scale characteristics of mature hurricanes. Part II: Inner core structure of Hurricane Allen (1980). *J. Atmos. Sci.*, **41**, 1287–1311.
- Kaplan, J., and M. DeMaria, 2003: Large-scale characteristics of rapidly intensifying tropical cyclones in the North Atlantic basin. *Wea. Forecasting*, **18**, 1093–1108.
- Kelley, O. A., J. Stout, and J. B. Halverson, 2004: Tall precipitation cells in tropical cyclone eyewalls are associated with tropical cyclone intensification. *Geophys. Res. Lett.*, **31**, L24112, doi:10.1029/2004GL021616.
- Keptert, J. D., and Coauthors, 2006: Tropical cyclone inner core dynamics. *Proc. Sixth Int. Workshop on Tropical Cyclones (IWTC-VI)*, San Jose, Costa Rica, WMO, 464–492.
- Kidder, S. Q., M. D. Goldberg, R. M. Zehr, M. DeMaria, J. F. W. Purdom, C. S. Velden, N. C. Grody, and S. J. Kusselson, 2000: Satellite analysis of tropical cyclones using the Advanced Microwave Sounding Unit (AMSU). *Bull. Amer. Meteor. Soc.*, **81**, 1241–1259.
- Knaff, J. A., S. A. Seseske, M. DeMaria, and J. L. Demuth, 2004: On the influences of vertical wind shear on symmetric tropical cyclone structure derived from AMSU. *Mon. Wea. Rev.*, **132**, 2503–2510.
- Lee, W. C., P. Dodge, F. D. Marks Jr., and P. H. Hildebrand, 1994: Mapping of airborne Doppler radar data. *J. Atmos. Oceanic Technol.*, **11**, 572–578.
- Malkus, J., and H. Riehl, 1960: On the dynamics and energy transformations in steady-state hurricanes. *Tellus*, **12**, 1–20.
- Mallen, K. J., M. T. Montgomery, and B. Wang, 2005: Reexamining the near-core radial structure of the tropical cyclone primary circulation: Implications for vortex resiliency. *J. Atmos. Sci.*, **62**, 408–425.
- Marks, F. D., and R. A. Houze Jr., 1987: Inner core structure of Hurricane Alicia from airborne Doppler radar observations. *J. Atmos. Sci.*, **44**, 1296–1317.
- , P. G. Black, M. T. Montgomery, and R. W. Burpee, 2008: Structure of the eye and eyewall of Hurricane Hugo (1989). *Mon. Wea. Rev.*, **136**, 1237–1259.
- Möller, J. D., and M. T. Montgomery, 1999: Vortex Rossby waves and hurricane intensification in a barotropic model. *J. Atmos. Sci.*, **56**, 1674–1687.
- Montgomery, M. T., and R. J. Kallenbach, 1997: A theory for vortex Rossby waves and its application to spiral bands and intensity changes in hurricanes. *Quart. J. Roy. Meteor. Soc.*, **123**, 435–465.
- , and J. Enagonio, 1998: Tropical cyclogenesis via convectively forced vortex Rossby waves in a three-dimensional quasi-geostrophic model. *J. Atmos. Sci.*, **55**, 3176–3207.

- , M. E. Nicholls, T. A. Cram, and A. Saunders, 2006: A vortical hot tower route to tropical cyclogenesis. *J. Atmos. Sci.*, **63**, 355–386.
- Nolan, D. S., and L. D. Grasso, 2003: Nonhydrostatic, three-dimensional perturbations to balanced, hurricane-like vortices. Part II: Symmetric response and nonlinear simulations. *J. Atmos. Sci.*, **60**, 2717–2745.
- , Y. Moon, and D. P. Stern, 2007: Tropical cyclone intensification from asymmetric convection: Energetics and efficiency. *J. Atmos. Sci.*, **64**, 3377–3405.
- OFCM, 1993: National hurricane operations plan. Office of the Federal Coordinator for Meteorological Services and Supporting Research, 125 pp. [Available from the Office of the Federal Coordinator for Meteorological Services and Supporting Research, Suite 1500, 8455 Colesville Rd., Silver Spring, MD 20910.]
- Reasor, P. D., M. T. Montgomery, F. D. Marks Jr., and J. F. Gamache, 2000: Low-wavenumber structure and evolution of the hurricane inner core observed by airborne dual-Doppler radar. *Mon. Wea. Rev.*, **128**, 1653–1680.
- , —, and L. F. Bosart, 2005: Mesoscale observations of the genesis of Hurricane Dolly (1996). *J. Atmos. Sci.*, **62**, 3151–3171.
- , M. D. Eastin, and J. F. Gamache, 2009: Rapidly intensifying Hurricane Guillermo (1997). Part I: Low-wavenumber structure and evolution. *Mon. Wea. Rev.*, **137**, 603–631.
- Riehl, H., and J. S. Malkus, 1958: On the heat balance in the equatorial trough zone. *Geophysica*, **6**, 503–538.
- Schubert, W. H., and J. J. Hack, 1982: Inertial stability and tropical cyclone development. *J. Atmos. Sci.*, **39**, 1687–1697.
- , C. M. Rozoff, J. L. Vigh, B. D. McNoldy, and J. P. Kossin, 2007: On the distribution of subsidence in the hurricane eye. *Quart. J. Roy. Meteor. Soc.*, **133**, 595–605.
- Shapiro, L. J., and H. Willoughby, 1982: The response of balanced hurricanes to local sources of heat and momentum. *J. Atmos. Sci.*, **39**, 378–394.
- Simpson, J., J. B. Halverson, B. S. Ferrier, W. A. Petersen, R. H. Simpson, R. Blakeslee, and S. L. Durden, 1998: On the role of “hot towers” in tropical cyclone formation. *Meteor. Atmos. Phys.*, **67**, 15–35.
- Spencer, R. W., and W. D. Braswell, 2001: Atlantic tropical cyclone monitoring with AMSU-A: Estimation of maximum sustained wind speeds. *Mon. Wea. Rev.*, **129**, 1518–1532.
- , R. E. Hood, F. J. LaFontaine, E. A. Smith, R. Platt, J. Galliano, V. L. Griffin, and E. Lobl, 1994: High-resolution imaging of rain systems with the Advanced Microwave Precipitation Radiometer. *J. Atmos. Oceanic Technol.*, **11**, 849–857.
- Steranka, J., E. B. Rodgers, and R. C. Gentry, 1986: The relationship between satellite-measured convective bursts and tropical cyclone intensification. *Mon. Wea. Rev.*, **114**, 1539–1546.
- Tory, K. J., M. T. Montgomery, and N. E. Davidson, 2006: Prediction and diagnosis of tropical cyclone formation in an NWP system. Part I: The critical role of vortex enhancement in deep convection. *J. Atmos. Sci.*, **63**, 3077–3090.
- Turk, J., F. S. Marzano, and A. Mugnai, 1998: Effects of degraded sensor resolution upon passive microwave retrievals of tropical precipitation. *J. Atmos. Sci.*, **55**, 1689–1705.
- Ulbrich, C. W., and P. B. Chilson, 1994: Effects of variations in precipitation size distribution and fallspeed law parameters on relations between mean Doppler fallspeed and reflectivity factor. *J. Atmos. Oceanic Technol.*, **11**, 1656–1663.
- Wakimoto, R. M., W.-C. Lee, H. B. Bluestein, C.-H. Liu, and P. H. Hildebrand, 1996: ELDORA observations during VORTEX 95. *Bull. Amer. Meteor. Soc.*, **77**, 1465–1481.
- Willoughby, H. E., 1998: Tropical cyclone eye thermodynamics. *Mon. Wea. Rev.*, **126**, 3053–3067.
- , and M. B. Chelmon, 1982: Objective determination of hurricane tracks from aircraft observations. *Mon. Wea. Rev.*, **110**, 1298–1305.
- , J. A. Clos, and M. G. Shoreibah, 1982: Concentric eye walls, secondary wind maxima, and the evolution of the hurricane vortex. *J. Atmos. Sci.*, **39**, 395–411.
- Zipser, E. J., 2003: Some views on “hot towers” after 50 years of tropical field programs and two years of TRMM data. *Cloud Systems, Hurricanes, and the Tropical Rainfall Measuring Mission (TRMM)—A Tribute to Dr. Joanne Simpson*, Meteor. Monogr., No. 51, Amer. Meteor. Soc., 49–58.